IMAGE: A MAP OF THE STARS OF THE ORION CONSTELLATION

Print ISSN: 2631-8474 Online ISSN: 2631-8482

JournalPreview

London Journal of Engineering Research

Volume 23 | Issue 1 | Compilation 1.0

Great Britain Journals Press

WWW.JOURNALSPRESS.COM

JournalPreview

LONDON JOURNAL ENGINEERING RESEARCH

Journal Content
In this Issue

Great Britain Journals Press

High-Resolution Road Segment Analysis using a Multi-Sensor Road Quality Classification System

Roland Nagy & István Szalai

University of Pannonia

ABSTRACT

Vibrations in road vehicles, mainly from road defects, have a number of harmful effects. Occupants may suffer health problems, while vehicle components may be mechanically damaged. These effects can reduce the life of components, cause failures and ultimately lead to vehicle breakdown. From a health point of view, back pain, liver injury and musculoskeletal problems are common, and body vibrations and shaking can negatively affect ride comfort.

The greatest negative impact is caused by a small number of large, isolated road defects, which generate low frequency but high amplitude vibrations. Related to this, our study aims to develop and implement a vibration-based road quality measurement system capable of detecting and differencing these prominent road defects.

Keywords: road quality measurement, vibration, classification, sensor fusion.

Classification: DDC Code: 629.231 LCC Code: TL243

Language: English

Great Britain Journals Press

LJP Copyright ID: 392941
Print ISSN: 2631-8474
Online ISSN: 2631-8482

London Journal of Engineering Research

Volume 23 | Issue 1 | Compilation 1.0

High-Resolution Road Segment Analysis using a Multi-Sensor Road Quality Classification System

Roland Nagy[α] & István Szalai[σ]

ABSTRACT

Vibrations in road vehicles, mainly from road defects, have a number of harmful effects. Occupants may suffer health problems, while vehicle components may be mechanically damaged. These effects can reduce the life of components, cause failures and ultimately lead to vehicle breakdown. From a health point of view, back pain, liver injury and musculoskeletal problems are common, and body vibrations and shaking can negatively affect ride comfort.

The greatest negative impact is caused by a small number of large, isolated road defects, which generate low frequency but high amplitude vibrations. Related to this, our study aims to develop and implement a vibration-based road quality measurement system capable of detecting and differencing these prominent road defects.

The implemented device is universally applicable to passenger vehicles, can be constructed at low cost and is controllable from a touch screen. The system includes inertial and GPS sensors, and various feature extraction and sensor fusion methods were used to fine-tune the results. The system has been tested and validated under real measurement conditions using measurement data collected on public roads.

Keywords: road quality measurement, vibration, classification, sensor fusion.

Author α: Institute of Mechatronics Engineering and Research, University of Pannonia, Gasparich Márk st. 18/A, H-8900, Hungary.
α σ: Mechatronics and Measurement Techniques Research Group, University of Pannonia, Egyetem st. 10, H-8200 Veszprém, Hungary.
*Corresponding author: Roland Nagy; nagy.roland@mk.uni-pannon.hu

I. INTRODUCTION

Vibrations on different frequencies and amplitudes occur in all moving vehicles, whether they are passenger cars or commercial vehicles. Efforts to dampen these vibrations have been made since the beginning of the automotive industry, as vibrations have a negative impact on both the mechanical system and the occupants of the vehicle. Vibrations can significantly reduce the lifetime of solder joints in the vehicle's electronic components and of the various mechanical assemblies, such as the internal combustion engine, steering gear or chassis. The degradation effect is significantly increased if the frequency of the vibration is the same as the natural frequency of a component. For people travelling in motor vehicles, vibration can cause long-term pathological changes, where the frequency of vibration is also a determining factor, with different frequencies being absorbed by different tissues and organs. Consequently, neurological and musculoskeletal disorders are common, and many people report spinal pain. Vibrations between 4 and 8 Hz are the most dangerous for the human body. [1] [2]

The vibrations mentioned so far may originate from motor vehicles, especially internal combustion engines, and may be caused by road surfaces and road defects. The latter is the more important cause, so our work will focus on road surface defects. Because of the important role of vibrations in vehicles, it is essential to know the condition and characteristics of the road network.

These up-to-date databases can also assist in the scheduling of road rehabilitation and maintenance works, which is essential for cost-effective and efficient planning.

Major and relatively deep surface defects, such as surface delamination or potholes, are of

particular importance as they have the highest damaging effect. These irregularities can cause high amplitude, low frequency vibrations in the vehicle, which are the most damaging from a mechanical and health point of view. Such defects are usually isolated on individual road sections and therefore need to be repaired individually. Furthermore, pave- ment separation type defects typically develop over a short period of time as a result of high forces. To effectively repair individual road defects, it is necessary to know the exact location of these defects, which can be achieved by an automated vehicle-mounted measurement system that allows high-resolution monitoring of individual road sections. However, the systems commonly available in the field are often expensive and difficult to obtain. [1] [3]

Due to these problems, our goal was to design and develop a system with a simpler architecture, which can be implemented at low cost, and where the desired detection accuracy is provided by sensor fusion. The output of the system should selectively indicate major surface road defects requiring urgent repair. The data should also include the position of each defect with good accuracy.

This paper is organized as follows. Section 2 will review the related works with possible implementations and key issues. Section 3 presents the development of the mechanical and software components of the system, together with the sensor fusion and machine learning steps used. Results and discussion are presented in Section 4, followed by a summary in Section 5.

II. RELATED WORKS

Several approaches have been developed to measure the quality of the road surface to meet the needs. Commonly used solutions are imaging with cameras or LIDAR sensors or 3D mapping of the pavement. These allow detailed and highly accurate mapping of the envelope, but have the disadvantage of expensive sensors and large data overheads, which can cause problems in evaluation and can be time-consuming. In addition, the use of these measurement systems and the mounting of the units typically requires custom-built vehicles. [4] A simpler method of measurement is to infer pavement defects from vibrations in the vehicle, which is the optimal solution in our case. The vibration-based methods are described below.

The dynamics of a general body of a passenger car can be described using a standard quarter-car model. The model is a simplification of the whole vehicle structure, but it describes its behaviour well. The equations thus written establish a relationship between the road surface characteristics and the vehicle suspension and body. Here, the suspension is referred to as unsprung mass and the vehicle body as sprung mass. The model also includes the characteristics of the tyre and spring, shock absorber.

Quarter-car model for a standard passenger car is shown in Fig.1. According to the transfer functions that can be written between the road surface characteristics as the input of the system and the sprung and unsprung masses as the output of the system, the road surface mainly determines the vertical accelerations at the output. Further studies confirm that movements due to road defects can also generate longitudinal or transverse vibrations in the vehicle body. [5] [6]

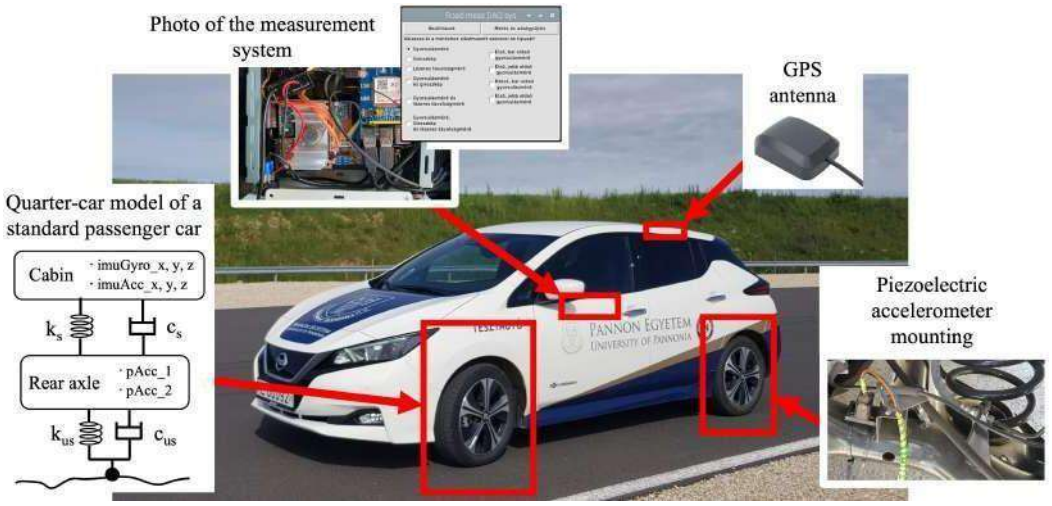

Figure 1: Picture of the Test Vehicle and the Developed Road Quality Measurement System With a Standard Quarter-Car Model and the Applied Markings

Vibration-based road quality measurement has the advantage of simpler sensor requirements and a more compact measurement system. Vibrations can be detected using lower cost accelerometers, most commonly analogue piezoelectric or digital MEMS and capacitance variation based types.

The latter can usually be achieved in an enclosure with a gyroscope and magnetometer sensor, also called an inertial measurement unit or IMU sensor. These sensors can detect acceleration, angular acceleration and magnetic field strength along a total of 9 axes. The movements in a vehicle body can be well described by the above data, allowing road quality measurements to be made using a few sensors. These methods are collectively referred to as response-based measurement methods. By fusing multiple sensor data sets, the results can be further refined. [7] [8]

Many works related to road quality measurement in the literature perform the measurement and data pro- cessing according to different methodologies. Study number [9] provides a good summary of response-based measurement methods. They divided the studies into three parts, distinguishing between Road Profile Recon- struction i.e. road roughness classification, Pothole Detection and Roughness Index Estimation. In the latter case, the road surface is characterised by means of some generated index, the most common of which is the Inter- national roughness - IRI index.

However, the disadvantage of these indices may be that they do not reflect well on individual but major road defects, but give a general estimate for a given road section. This limits their potential for higher resolution monitoring. The IRI index is usually only calculated for sections greater than 100 m. In Pothole Detection work, the general objective is to detect road defects exceeding a certain parameter, whereas in Profile Reconstruction work, roads are characterised by the calculation of different features, but in these cases the classified sections are composed of small sections, even smaller than 1 metre. Thus, in our research we decided to use these methods.

Power Spectral Density (PSD) has been shown to be a good indicator, providing a good correlation between road unevenness and vehicle or human body ride vibration. [10] [11] A PSD function transforms a signal from the time domain to the frequency domain and provides its frequency spectrum. Digital signal processing provides many possibilities for this, such as Fast Fourier Transform (FFT). The frequency information of the vibration signal than refers to the power of the vibration data over time. The advantage of this is that the small pulse-like effects in the signal are well represented.

A number of different methods are used for the subsequent evaluation process. Some have used a Support Vector Machine (SVM) classification model to classify each stage. This has achieved an average accuracy of 98%. Neural network based Multi-Level Perception (MLP) and decision tree based algorithms have also been tested and have also produced good results. In addition to the vibration data, GPS units were used to collect position data for later locating data points. [7]

Several studies have also focused on the dependence of vibration data on vehicle speed. According to these, a variation in vehicle speed can affect the frequency and amplitude of the measured wheel acceleration, this would introduce relevant errors in the results without correction. No general correction factor can be defined to correct these errors, as the vibrations that occur also depend on the damping factors of the vehicle. In [6] a spatial frequency based resampling was applied, which also greatly reduced this speed dependence. The method can also be used to increase the detection resolution, and we have therefore chosen to use this method in our work.

Spatial based resampling can be done using GPS coordinates, where the location of new data points is defined as a function of distance instead of time. The new values can be acquired by interpolation, where specific query points are defined at arbitrary distances Δs and then the interpolated $z(s)$ values are calculated from the original $z(s)$ points. By Shannon's law, the chosen Δs then determines the maximum spatial frequency, and hence the maximum resolution. Δs is mainly determined by frequency domain considerations. The spatial sampling frequency after the interpolation is

$$f_{spatial} = \frac{1}{\Delta s}$$

The sampling frequency gives the Nyquist frequency, which specifies the highest spatial frequency that can be resolved from the vibration data and therefore corresponds to the minimum road irregularity size still detectable after processing. It value can be calculated as follows

$$f_{Nyquist} = \frac{1}{2\triangle s} = \frac{f_{spatial}}{2} \quad (2)$$

We will further use this background to further define the parameters of the interpolation and explore different optimization options in the discussion.

Some studies have also investigated the effect of sensor placement on measurement accuracy.

While in-cab measurement alone can simplify the measurement system design, the quarter-car model suggests that the damping elements in the suspension can significantly distort and isolate the vibrations. Some of the vibrations generated will be transmitted to the vehicle body, but the frequency of the remaining vibrations will also be altered by the system. The shock absorber elements usually distort the high frequency vibrations for the most, which are the most critical from a mechanical failure and health point of view. Thus, the accuracy of the measurement can be greatly increased by placing additional sensing elements on the unsprung mass. Some studies have also addressed the effect of the tyre, but its damping effect is negligible compared to the 0.2 - 0.4 damping ratio of the spring and damper.

III. ARCHITECTURE OF THE MEASUREMENT SYSTEM AND DATA PROCESSING UNIT

These are the basis on which we have constructed the system presented in this chapter. After the hardware architecture, the development of the software data processing algorithms is discussed.

3.1 Hardware Structure of the Unit

The measuring device is based on a Raspberry PI 4 microcomputer, which provides the control of the hardware components, data storage and external peripherals. The single-board computer has sufficient computing power to control multiple external microcontrollers and to implement communication, has directly accessible digital connectors supporting common communication standards, and can be connected to a touchscreen via USB and HDMI connectors.

Road surface defects are detected using two different types of sensors, and for the above reasons, vibrations were measured on both the unsprung and sprung masses. Piezoelectric acceleration sensors of type 805M1-0020 are placed on the vehicle undercarriage to directly detect displacements due to road surface roughness and the resulting acceleration. These sensors are placed on the trailing arms at the rear of the vehicle, so damping elements have less influence on the measurement results. The movements of the vehicle body, or the sprung mass, are detected by an inertial measurement unit (IMU) of type MPU6050 installed in the passenger compartment. The sensor unit includes a 3-axis accelerometer and a 3-axis gyroscope sensor. These data are used to isolate major road defects and sensor fusion methods are used to reduce the impact of vehicle manoeuvres such as cornering and braking on the measured data. The labelling used for each sensor is shown in Fig.1.

The analogue outputs of piezoelectric accelerometers are connected to individually designed signal conditioning circuits containing amplifier, offset and filter elements. The optimised analogue signal is digitised by a 12-bit MAX186 A/D converter, which provides a resolution of 1.22 mV resolution of the input signal in the range 0 - 5 V. The output of the converter is available via SPI and I2C communication, so an ATmega328 microcontroller is used to read the digitized values, and creating a data buffer to reduce the load on the Raspberry PI unit and increase the sampling rate. The I2C communication protocol provides the connection between the microcontroller, the additional sensors and the Raspberry PI in a single-master, multi-slave system. Since the microcontroller operates at 3.3 V and the additional components at 5 V, the communication is established by inserting a dual-channel level shifter circuit. During the measurements, the position data is recorded using a Waveshare SIM7600 type GPS module, which is directly connected to the Raspberry control unit. The sampling frequency of the measurement system is 160 Hz, while the position data are recorded by the device at a frequency of 10 Hz. In addition to the data acquisition and recording elements, we have designed a power supply to fit the system. Its input voltage range of 7.5 V to 35 V allows operation from a car cigarette lighter socket. The picture of the developed system and the mounting to the test vehicle is shown in Fig.1.

3.2 Data Processing and Classification Algorithm

After the design and construction of the hardware units, the software parts were developed, which are presented in this subsection. The algorithm provides the sensor fusion and then evaluates the aggregated data based on a classification model, creating an easily interpretable 1-dimensional objective output. The presented algorithms are developed in a Matlab software environment.

First, the array of 8 data series obtained from the measured values is imported, and then basic signal processing steps are performed to reduce the effect of erroneous values and noise. The raw data series after import are shown in Fig.2. This involves correcting for trend or drift errors using the detrend method. The stationary data series is generated by curve fitting to the values. In practice, typical accelerometers have near-constant measurement biases which, if not compensated, can cause large deviations in subsequent steps. Thus, in addition to removing trend-like errors, attention was also paid to correcting for biases. For the selection and removal of gross error values, a lower and upper bound tolerance band was defined, outside which values were removed from the data set. The limit is defined as three times the standard deviation, with values outside this limit being only 0.27% of the total data according to the normal distribution. In addition, since the GPS sampling frequency was lower than the sampling frequency of the accelerometers, missing data points were made up for by interpolation.

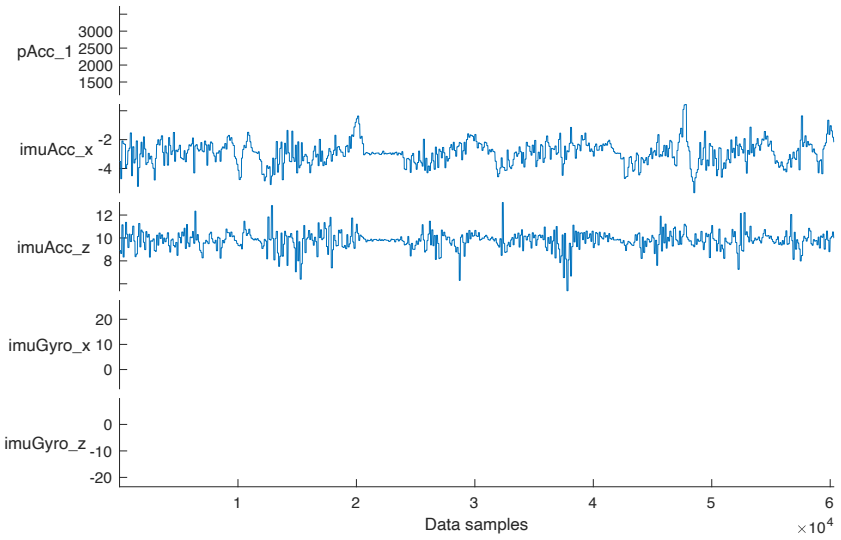

Figure 2: Imported Raw Data From Specific Accelerometer and Gyroscope Sensors Before Signal Processing

The feature extraction aims to reduce the dimension of the initial data block. In this process, we search for features that describe the information content of the original data set with good accuracy and completely. After the signal processing steps, the data points were resampled as a function of distance to reduce the velocity dependence and to achieve the appropriate resolution. For this purpose, the new data points were recorded at a distance of Δs = 0.025 m, resulting in a spatial Nyquist frequency of 20 m−1.

With this parameter we also define the resolution of the data acquisition. Based on [12] and [13], single envelope defects of significant size are typically 10-30 cm in extent, thus the resolution determined is sufficient to detect them. A power spectrum is calculated from the resampled data points using Fast Fourier Transform. The results are plotted on a spectrogram, which clearly shows the high power data points as a function of distance travelled and spatial frequency, which may indicate the road defects to be detected. The spectrogram also allows us to select a band within the full spatial frequency range where the largest change occurs. As this has the highest information content, it is highlighted in the following, thus reducing the size of the data table.

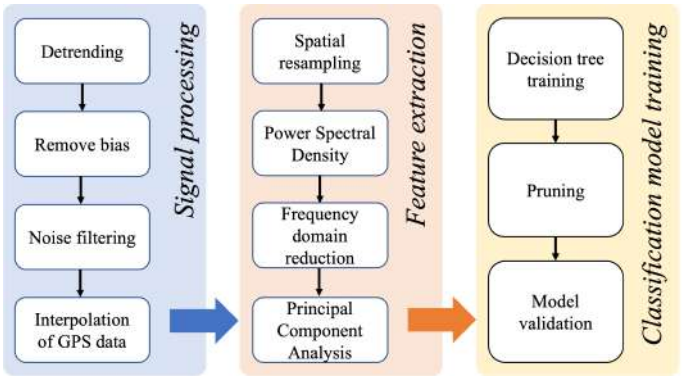

Figure 3: Flowchart of the Matlab Classification Algorithm

In the next step, Principal Component Analysis was used to distinguish outliers and to examine the correlation of the individual sensor data. The searched values were already well separated from the points around the mean as a function of the first principal component. These PCA scores were

used to train a classification model using a decision tree. The model allows us to classify data points into different classes based on objective criteria and also provides a sensor fusion. In the classification process, each data point representing a road segment is classified into 2 classes, where Class 1 represents major road defects requiring urgent intervention. Sections classified in Class 2 are not necessarily free of failures, but only irregularities of minor extent or depth occur. During model training, the accuracy of the output was validated by 10-fold cross-validation and the tree size was reduced by pruning. By cross-validation, a classification accuracy of 96% was obtained. The flowchart of the implemented data processing and classification algorithm is shown in Fig.3

IV. RESULTS AND DISCUSSION

Following the construction of the measurement system, a series of tests were carried out under real-world condi- tions. These tests focused on the reliability and the accuracy of the system. This chapter summarises the results of these tests.

Figure 4: Reference Photos of the Pavement Failure Classes We Focus On; A) Pothole, B) Manhole Depression and C) Surface Delamination

The measuring instrument was mounted on an electric-drive 2019 Nissan Leaf vehicle, as shown in Fig.1. Due to the high resolution, the measurements were largely performed within a populated area, choosing routes as varied as possible. In total, over 70 km of data were collected under varying weather conditions. The previously presented road irregularity types to be detected, which are the focus of this study, are shown in Fig.4and include deeper potholes, manhole depression and pavement delamination.

The advantage of the system and the sensors used is that external conditions did not affect the operation or usability of the system. During the measurements, the speed varied between 0 km h−1 and 70 km h−1. The results were plotted on maps.

The first presented results are shown in Fig.5with a map, where the blue colour indicates the location of major pavement defects, and the yellow colour indicates the sections free of these defects. As can be observed, the section under study is largely free of major anomalies, although a few characteristic points have been detected.

The section marked in red circle was the most affected by large surface irregularities, with wider potholes and depressions and asphalt folding. The classification of the data corresponded to our visual observation, with the locations of the indicated road defects corresponding to reality.

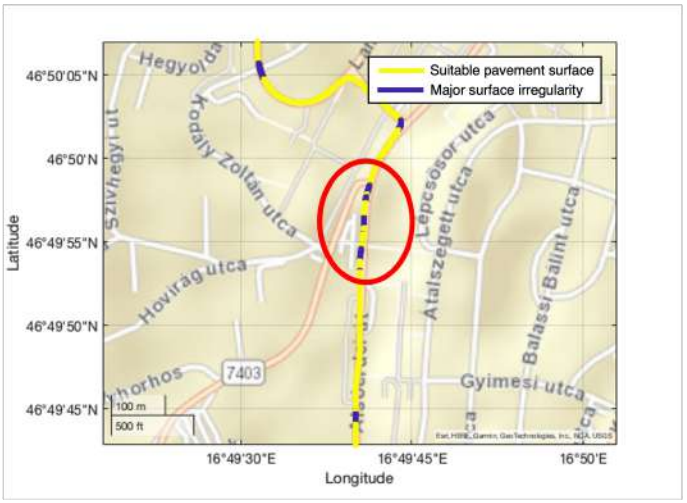

Figure 5: Classification Results on a Relatively Well Maintained Road Section in an Urban Environment

Fig. 6 also shows the results of a measurement in an urban environment. From these data, mainly coherent sections can be distinguished, with significant road surface defects being present together. In these areas, deeper potholes and surface delamination were largely present. In between the contiguous poor areas were sections of improved and repaired asphalt overlay in highlighted yellow locations.

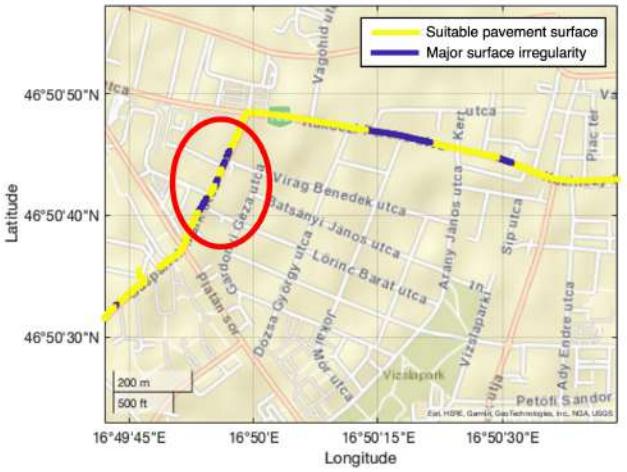

Figure 6: Classification Results for Areas With Quality-Related Coherent Sections

The results of the last measurement presented are shown in Fig.7, also in an urban environment, at a speed of approximately 60 km h−1. On this section, a generally good quality road surface was observed, but in addition a large number of separate surface defects of small extent were observed. Examples included depressions at the manhole cover and deeper potholes, which are common in many urban environments. These individual road defects detected are highlighted in the red circle on the map showing the classification results. The detected position of the road defects corresponds to our real experience based on GPS data.

In general, the measurement results are consistent with our expectations and visual observations. The detected defects were a good representation of the real road conditions and the classification results provided a good identification of the major poor road sections encountered.

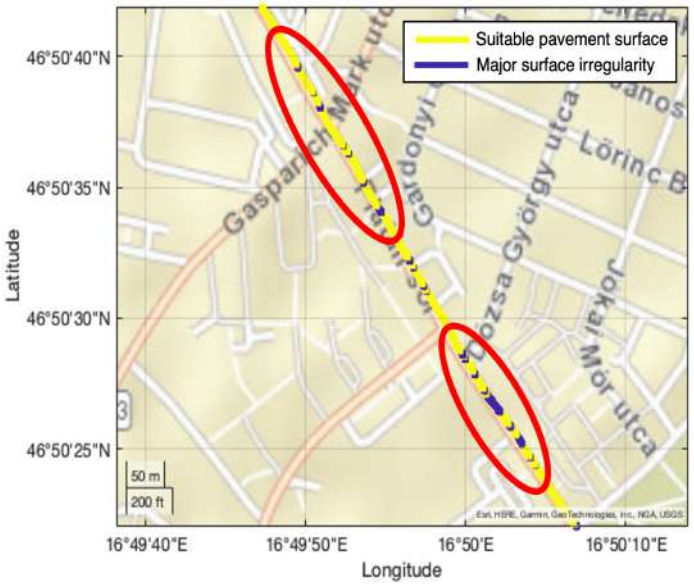

Figure 7: Classification Results on a Section Burdened With a Large Number of Discrete Road Surface Irregularities

V. SUMMARY

In this study, our objective was to design and test a measurement system capable of detecting separated, high negative impact road surface failures. These individual road defects typically have a high negative impact on both the vehicle mechanical units and the occupants, while monitoring the road network is a costly task. In this context, a universally and easily applicable low-cost system for passenger vehicles was designed. The unit detects surface irregularities using accelerometer and gyroscope sensors and saves them alongside GPS position data. The unit is easily operated from a GUI interface using a touch screen. The results are refined through advanced data processing steps using Power Spectral Density and Principal Component Analysis to extract information from the raw data.

A decision tree based classification model is taught for sensor fusion. The measurement system was tested under real conditions with data collected on public roads. The results showed good accuracy, with deeper road defects well observed. Furthermore, the evaluation of the large data tables was greatly facilitated by the system, which made the data processing process time efficient.

ACKNOWLEDGEMENTS

This work has been implemented by the TKP2020-NKA-10 project with the support provided by the Ministry of Culture and Innovation of Hungary from the National Research, Development and Innovation Fund, financed under the 2020 Thematic Excellence Programme funding scheme.

The program has been supported by the Zala ZONE Automotive Proving Ground Zala Ltd.

DECLARATION OF CONFLICTING INTERESTS

The authors declared that there are no potential conflicts of interest with respect to the research, authorship, and/or publication of this article.

REFERENCES

1. Nuno S, Vaibhav S, Joao S, Helena R (2018) Road Anomalies Detection System Evaluation. MDPI Sensors 18(7): 1–20.
2. Granlund J (2012) Vehicle and Human Vibration due to Road Condition. The ROADEX "Implementing Accessibility" Project 1–10.
3. Douangphachanh V and Oneyama H (2013) A Study on the Use of Smartphones for Road Roughness Con- dition Estimation. J-STAGE

Journal of the Eastern Asia Society for Transportation Studies 10: 1551–1564.
4. Mahlberg J A, Li H, Zachrisson B, Leslie D K and Bullock D M (2022) Pavement Quality Evaluation Using Connected Vehicle Data. Sensors 2022 22: 9109.
5. Wong J Y (2001) Theory of ground vehicles. John Wiley and Sons, Inc.
6. Ward C and Iagnemma K (2009) Speed-independent vibration-based terrain classification for passenger vehicles. Vehicle System Dynamics: International Journal of Vehicle Mechanics and Mobility 47(9):1095–1113.
7. Nuno S, Joao S, Vaibhav S, Maribel Y S, Helena R (2017) Anomaly Detection in Roads with a Data Mining Approach. Procedia Computer Science 121: 415–422.
8. Bello S, Aibinu A, Onwuka L, Dukiya J, Bima M, Onumanyi A, Folorunso T (2015) A New Measure for Analysing Accelerometer Data towards Developing Efficient Road Defect Profiling Systems. Journal of Sci- entific Research and Reports 7(2):108–116.
9. Nguyen T, Lechner B and Wong D Y (2019) Response-based methods to measure road surface irregularity: a state-of-the-art review. European Transport Research Review 11(43):1–18.
10. Mu´ˇcka P and Granlund J (2012) Comparison of Longitudinal Unevenness of Old and Repaired Highway Lanes. American Society of Civil Engineers: Journal of Transportation Engineering 138(3):371 –380.
11. Ahlin K and Granlund J (2002) Relating road roughness and vehicle speeds to human whole body vibration and exposure limits. International Journal of Pavement Engineering 3(4): 207–216.
12. Sayers M W, Gillespie T D and Paterson W D o (1986) Guidelines for Conducting and Calibrating Road Roughness Measurements. World Bank technical Paper (46).
13. Sayers M W, Gillespie T D and Queiroz C A V (1986) The International Road Roughness Experiment: A Basis for Establishing a Standard Scale for Road Roughness Measurements. Transportation Research Record 1084:76–85.

Analysis of Straight Stairs under Earthquake and Pedestrian Loads

Osama Salem Hussien

Al-Azhar University

ABSTRACT

Staircases connect the floors of multi-storey buildings and pedestrian bridges. There are different types of stairs, such as straight stairs, straight stairs with intermediate landings, curved stairs, L-shaped stairs, etc. The study focused on straight staircases with a central beam supporting the stairs as a double cantilever. The study of structural systems is relatively rare. There are four loading cases that we examine; the first is a live load on one side of the staircase, the second is a live load on both sides of the staircase, the third is a time history of three earthquakes, and the fourth is a dynamic load of pedestrians. A major objective of this study was to establish equations for estimating the central beam's internal forces.

Keywords: straight stair; dynamic loads; reinforced concrete beams; cases of loading; pedestrian load.

Classification: DDC Code: 331.1280973 LCC Code: HD5861

Language: English

Great Britain Journals Press

LJP Copyright ID: 392942
Print ISSN: 2631-8474
Online ISSN: 2631-8482

London Journal of Engineering Research

Volume 23 | Issue 1 | Compilation 1.0

Analysis of Straight Stairs under Earthquake and Pedestrian Loads

Osama Salem Hussien

ABSTRACT

Staircases connect the floors of multi-storey buildings and pedestrian bridges. There are different types of stairs, such as straight stairs, straight stairs with intermediate landings, curved stairs, L-shaped stairs, etc. The study focused on straight staircases with a central beam supporting the stairs as a double cantilever. The study of structural systems is relatively rare. There are four loading cases that we examine; the first is a live load on one side of the staircase, the second is a live load on both sides of the staircase, the third is a time history of three earthquakes, and the fourth is a dynamic load of pedestrians. A major objective of this study was to establish equations for estimating the central beam's internal forces.

Keywords: straight stair; dynamic loads; reinforced concrete beams; cases of loading; pedestrian load.

Author: Associate Professor, Civil Engineering Dept., Al-Azhar University, Cairo, Egypt. email: dreng134@yahoo.com, OsamaSalem.14@azhar.edu.eg

I. INTRODUCTION

Stairs are a critical topic in structural engineering, as they provide access between floors, whether in public markets, residential buildings, government departments, or pedestrian bridges. This is a brief overview of the history of stairways as they relate to different civilizations, architectural ideas, and structural designs. Wood trunks formed the stairs approximately 6000 years ago. Scientists discovered the first granite staircase leading to the sacred mountain in Tai Shan, China, and the spiral staircase in the Babel Tower, as well as screws stairs used for military purposes in castles, and straight stairs in Egyptian pyramids.

Peter Nicholson developed a mathematical method to improve handrail construction toward the end of the 19th century (at the peak of stair building). Towards the end of 1980, Eva Girishna from London designed an elegant set of stairs made of glass and stainless steel. www.britannica.com and www.elevestairs.com offer information about the history of stairs. We analyze the straight staircase with an intermediate landing. It consists of a beam in the middle of the slab. This beam is supported by a tie beam at the first, a column in the middle, and a cross beam at the end. This study aims to provide equations for the internal forces of the central beam. These equations will assist engineers in designing this staircase type.

Khaldoun N. (2001) presented an approach to the design and analysis of concrete beams subjected to purely torsional stresses. The accuracy of the method was very similar to that of the literature in the torsion and shear cases. Consequently, the method is applicable to torque problems under certain assumptions. In 2006, Zia W. and Sohrabuddin A. proposed a design aid for helicoidal stair slabs with intermediate landings. They found that landings had a significant effect on the vertical moment, torque, and lateral shear when present. Using full-sized prefabricated steel stair assemblies, Christopher H (2009) evaluated the seismic inter-story drift response with factored gravity loads. His conclusion was that the connections between stairs and landings provided some moment restraint that

reduced separation at those locations under lateral loads, and designers should consider these connections as simply supported.

Michael K. and Benjamin C. (2011) conducted two experiments. In the first experiment, they measured the load exerted by one foot for one step. The second experiment involved the loading caused by walking on a stair wing. Two steps at once resulted in significantly higher load amplitudes of the first two integer harmonics than one step alone, the researchers found. Brad D. and Onur A. (2015) proposed a simplified method for evaluating vertical vibrations below 10 Hz when ascending or descending slender stairs. Based on Yuxing Z's (2016) conclusion, statically determinate stairs exhibit sufficient redundancy and ductility in the main structure. Blazes R. and Katalin B. (2018) studied stone cantilever staircases for reconstruction and new construction. This study examines discrete element simulations of stair design in order to predict mechanical behavior.

Wang X. and Hutchinson T. (2018) examined the seismic response of scissor-operated stairs. During the pre-design stage of stairs, they believed that changes in connection details and geometrical shapes had a significant impact on seismic behavior. Jose S et al (2019) proposed a stiffness condition (K >= 3600 kN/m) that will eliminate the need for dynamic analysis by guaranteeing that excessive vibrations will not be experienced. Mahsa B. and Ehsan S. (2019) modelled a brick stair wall as a supporting structure for excavations under various conditions. Their findings indicate that the applied surcharge on the contiguous area of the stair wall significantly influences the evaluation of the damage.

The model of Ke Changren and Wang H (2020) used damp bearings to make the stairway earthquake-proof. They compared the advantages and disadvantages of three different staircase structures that differ in relation to the input seismic wave feedback. Based on the Maxwell mechanical model, they concluded that improved viscous damping bearings could change the uneven distribution of rigidity of the structure caused by the stairs. This would improve ductility and seismic performance.

Since our previous literature review did not identify what the behavior of a central beam supporting a stair as a double cantilever is, this paper investigates it.

II. CASE STUDY

Our lives include this type of staircase as shown in Fig. 1, and its details are shown in Fig. 2

Fig. 1: Photo of Stair

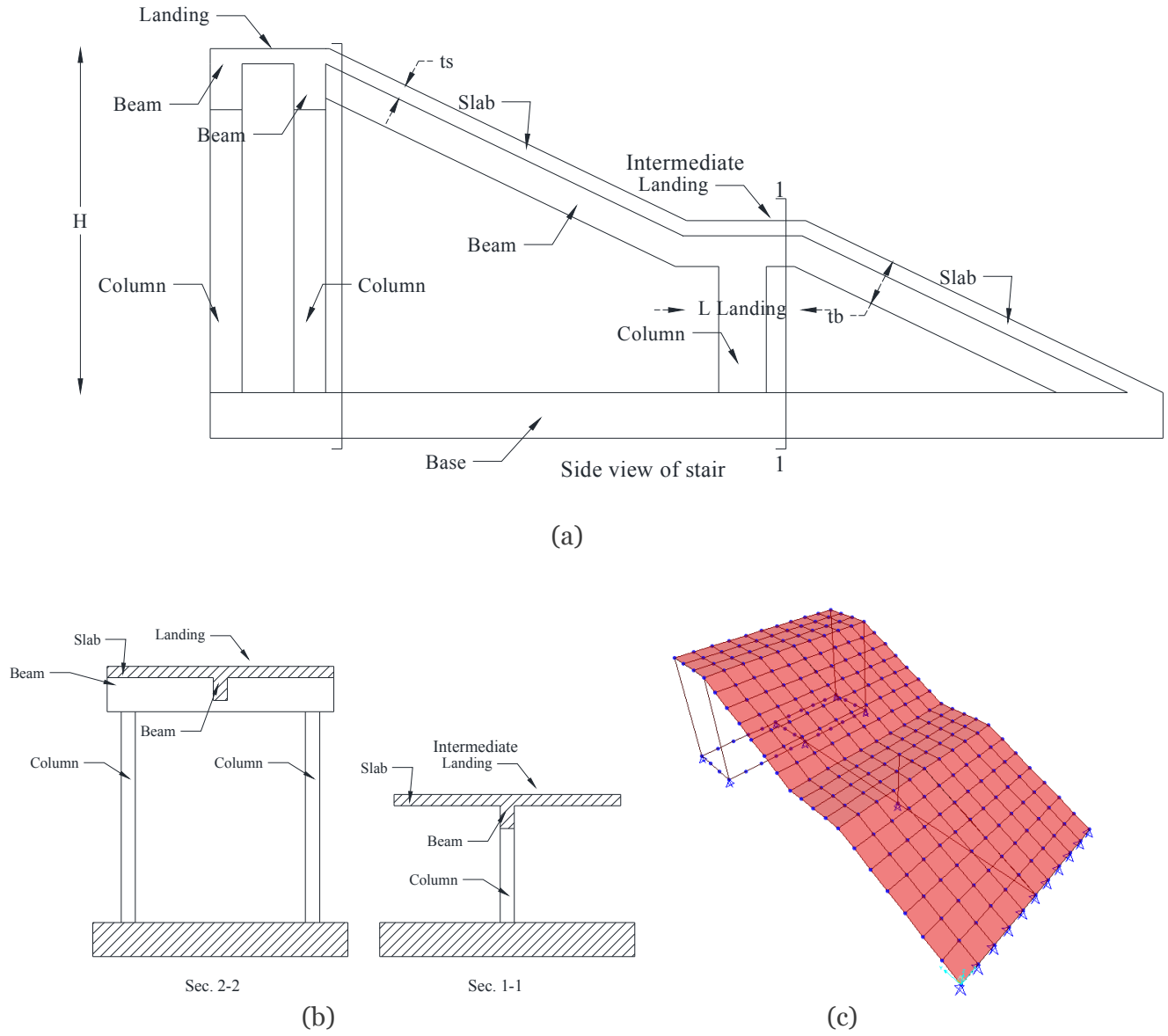

Fig. 2: Details of Staircase: (A) Side View of Stair, (B) Sections of Stair (C) the Model

Numerical techniques such as the finite element method (FEM) may be used to represent objects, such as stairs, as groups of elements or meshes. A final solution is found by combining the results of each element separately. A displacement function is assumed to describe displacements within the elements of the stair, rather than an infinite series. Fig. 2(c) shows the 3D model with finite element analysis of the central beam of the stair; the cross-section of the model can be seen in Fig. 2(b). A finite element analysis was performed using SAP software. Fig. 2(a) shows the model's layout, and Fig. 2(c) shows the stair's eight-node solid elements. This staircase has hinged support at its boundary conditions, as can be seen in Figure 2(c)

Design of the slab according to ACI 318-14. Assumptions for the design are as follows: live load is 0.480 t/m², reinforced concrete density is 2.5 t/m³, prismatic compressive strength is 2800 t/m², and yield strength is 42000 t/m². The stair dimensions are 1.50 m landing length, 3 m to 5 m stair height, and 2.0 m to 5.0 m stair width. The results of the design are shown in Fig. 3.

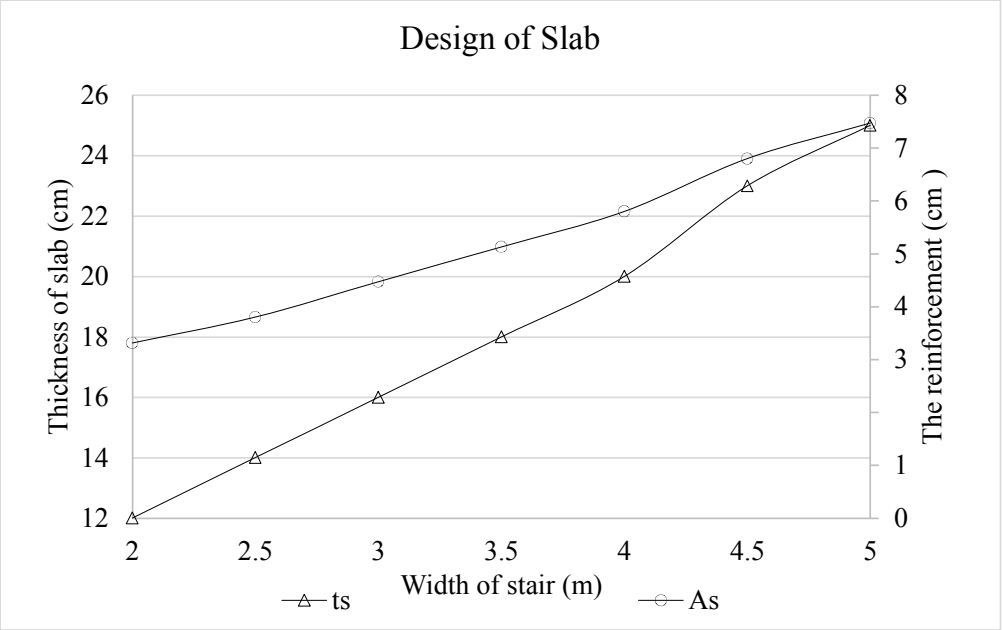

Fig. 3: The Relationship Between Stair Width, Slab Thickness, and the Reinforcement

Beam design according to ACI 318-14. There are four types of loading investigated, such as live loads on one side of the slab, live loads on both sides of the slab, time histories of earthquakes, and pedestrian dynamic loads. For determining maximum internal forces within the supporting beam, Figure 4 shows the times history analysis of three earthquakes (Sierra Madre, Loma Prieta, and Northridge-01). Axis X represents time and axis Y represents acceleration.

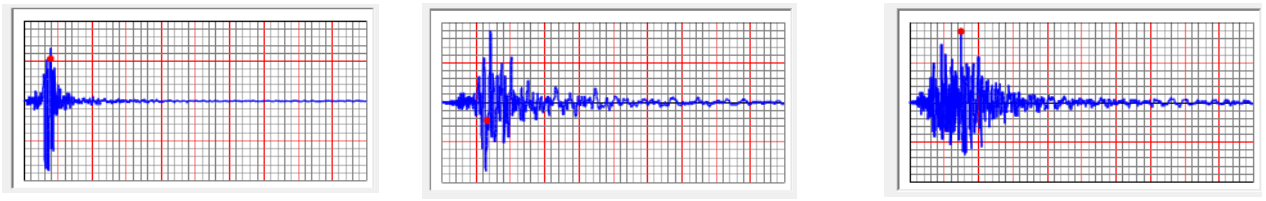

(a) Sierra Madre (b) Loma Prieta (c) Northridge-01

Fig. 4: Time History of Earthquakes

Details of earthquakes:

1. *Earthquake Name:* Sierra Madre, Station Name: Altadena - Eaton Canyon, Record Sequence Number: 1641, the magnitude is 5.6 occurred on June 28, 1991, at 7:43 PM.
2. *Earthquake Name:* Loma Prieta, Station Name: Hollister - South & Pine, Record Sequence Number: 776, the magnitude is 6.93 occurred on October 17, 1989, at 5:04 PM.
3. *Earthquake Name:* Northridge-01, Station Name: LA - Century City CC North, Record Sequence Number: 988, the magnitude is 6.69 occurred on January 17, 1994, at 4:31 AM.

Walking across the span of a stairway causes vibrations to occur. As a first step, we calculate the vertical pulsating force (F) and the distributed load (W) using equations 1 & 2 from Euro code 2003, and then apply these calculations to our model to calculate the dynamics.

$$F = F_0 . k(f_v) . \sqrt{1 + \gamma . (N - 1)} . \sin sin \left(2\pi . f_v . t\right) \qquad Eq. 1$$

$$w = 1.8\left(\frac{F_0}{A}\right).k\left(f_v\right).\sqrt{\gamma.N/\lambda}.\sin sin\ (2\pi.f_v.t) \qquad Eq.2$$

According to the stair data, F_o = 280 N for walking and crowds, while F_o = 910 N for jogging. This type of stair belongs to the class C (Urban routes subject to significant variation in daily usage). Group size for walking (N=8), for jogging (N=2), Crowd density ρ = 0.8 (person/m²). For walking and jogging cases, the coefficient γ is 0.8 when L=9.71 m, 0.562 when L=11.94 m and 0.489 when L=14.18 m, whereas for crowd case γ is 0.114. Tables (1) and (2) show the pulsating forces for walking and jogging, respectively, while Table (3) shows the pulsating distributed loads for crowds

Table 1: Vertical Pulsating Force for Walking Condition

b	L = 9.71 m, h = 3 m			L = 11.94 m, h = 4 m			L = 14.18 m, h = 5 m		
	f_n Hz	K(f_n)	Amplitude N	f_n Hz	K(f_n)	Amplitude N	f_n Hz	K(f_n)	Amplitude N
2 m	17.946			11.577			8.094	0.020	11.778
2.5 m	17.084			11.2			7.924	0.024	14.028
3 m	16.333			10.881			7.797	0.030	17.747
3.5 m	15.709	0.02	14.387	10.632	0.02	12.438	7.715	0.034	20.174
4 m	15.179			10.436			7.668	0.037	21.56
4.5 m	14.695			10.262			7.637	0.038	22.47
5 m	14.276			10.078			7.596	0.040	23.68

Table 2: Vertical Pulsating Force for Jogging Condition

b	L = 9.71 m, h = 3 m			L = 11.94 m, h = 4 m			L = 14.18 m, h = 5 m		
	f_n Hz	K(f_n)	Amplitude N	f_n Hz	K(f_n)	Amplitude N	f_n Hz	K(f_n)	Amplitude N
2 m	17.946			11.577			8.094		
2.5 m	17.084			11.2			7.924		
3 m	16.333			10.881			7.797		
3.5 m	15.709	0.02	24.4179	10.632	0.02	22.746	7.715	0.02	22.21
4 m	15.179			10.436			7.668		
4.5 m	14.695			10.262			7.637		
5 m	14.276			10.078			7.596		

Table 3: Vertical Pulsating Distributed Load for Crowd Condition

b	L = 9.71 m, h = 3 m					L = 11.94 m, h = 4 m					L = 14.18 m, h = 5 m				
	f_n Hz	K(f_n)	Area (m²)	N	Amplitude (N/m²)	f_n Hz	K(f_n)	Area (m²)	N	Amplitude (N/m²)	f_n Hz	K(f_n)	Area (m²)	N	Amplitude (N/m²)
2 m	17.946		19.4	16	1.107	11.577		23.9	20	1.007	8.094	0.020	28.4	23	0.909
2.5 m	17.084		24.3	20	0.990	11.2		29.9	24	0.882	7.924	0.024	35.5	29	0.973
3 m	16.333		29.1	24	0.904	10.881		35.8	29	0.808	7.797	0.030	42.6	35	1.127
3.5 m	15.709	0.02	34	28	0.837	10.632	0.02	41.8	34	0.750	7.715	0.034	49.6	40	1.173
4 m	15.179		38.8	32	0.783	10.436		47.8	39	0.703	7.668	0.037	56.7	46	1.177
4.5 m	14.695		43.7	35	0.728	10.262		53.7	43	0.656	7.637	0.038	63.8	52	1.161
5 m	14.276		48.6	39	0.692	10.078		59.7	48	0.624	7.596	0.040	70.9	57	1.151

The frequency values in Tables 1, 2, and 3 decreased by an average of 3.74%, 2.28%, and 1.05%, respectively, at 3, 4 and 5m of stair height, corresponding to an increase of stair breadth of 25% of the original value. In addition, the frequency values decrease by an average of 32.79%, 31.85%, 30.86%,

29.88%, 28.89%, 27.87% and 27.02%, corresponding to an increase of stair height by 33.3% of the original value, at 2, 2.5, 3, 3.5, 4, 4.5 and 5m of stair breadth respectively. The values of K (f_v) are constant above 8 Hz for walking and 7 Hz for jogging and increase as the frequency value decreases beneath the previous values. There is a direct relationship between amplitude and γ and K (f_v), and amplitude increases as these parameters increase.

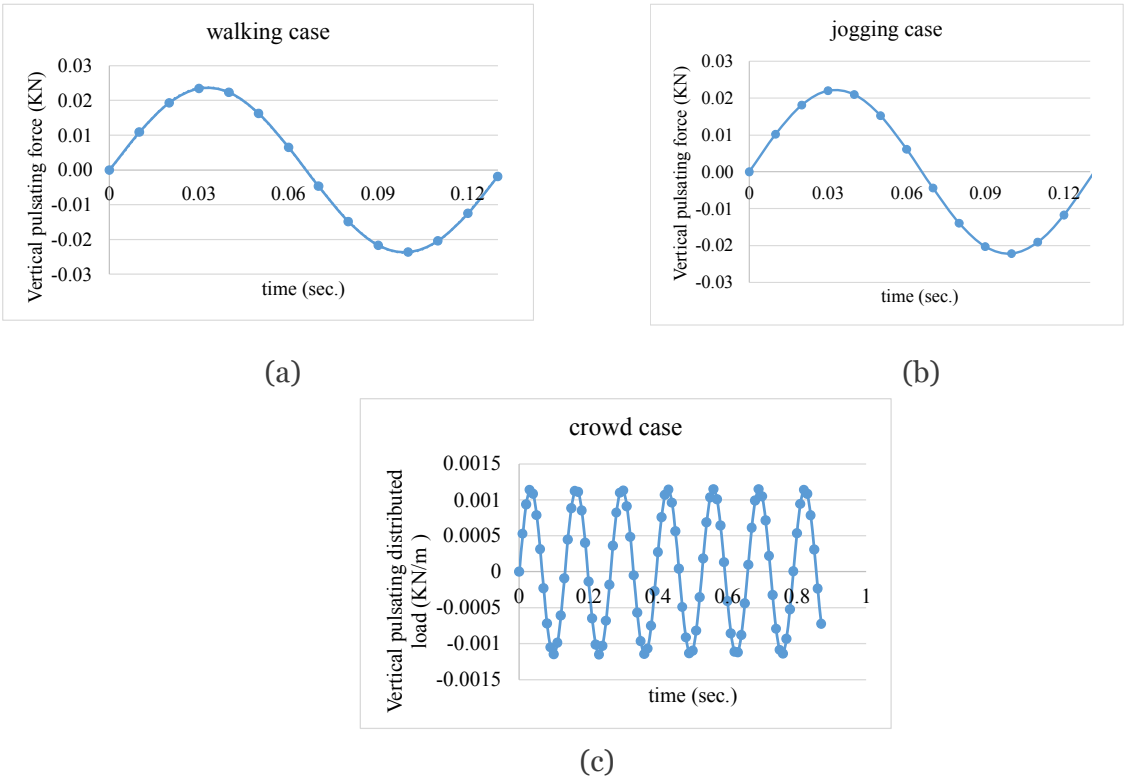

Fig. 5: Vertical Pulsating Force for (A) Walking Case, (B) Jogging Case and (C) Vertical Pulsating Distributed Load for Crowd Case

As shown in Figure 5 (a & b), the vertical pulsating force for walking and jogging is distributed with time. For the crowd case, Figure 5c shows the vertical pulsating distributed load distribution with time. The codes have three categories of movement: walking, jogging, and crowds. Walking has a speed of 1.7 m/s, jogging has a speed of 3 m/s, and crowds have a speed of 1.7 m/s. Based on the Euro code, the pedestrian comfort criteria have two conditions: first, the deck's fundamental frequency is greater than 5 Hz for vertical vibrations and 2.5 Hz for lateral and torsional vibrations. Second, the comfort acceleration of any portion of the deck, which should not exceed 0.7 m/s2 for vertical vibrations, 0.2 m/s2 for horizontal vibrations resulting from regular use, and 0.4 m/s2 for exceptional crowding.

III. RESULTS

This study examined five load combinations. First, is the dead load and live load, second is the dead load and live load on one side, third is the dead load and live load with the earthquake, fourth is the dead load and live load on one side with the earthquake, and fifth is the dead load and dynamic load of the pedestrian. Our analysis of the beam involved the use of the critical combination.

a) Effect of the pedestrian load

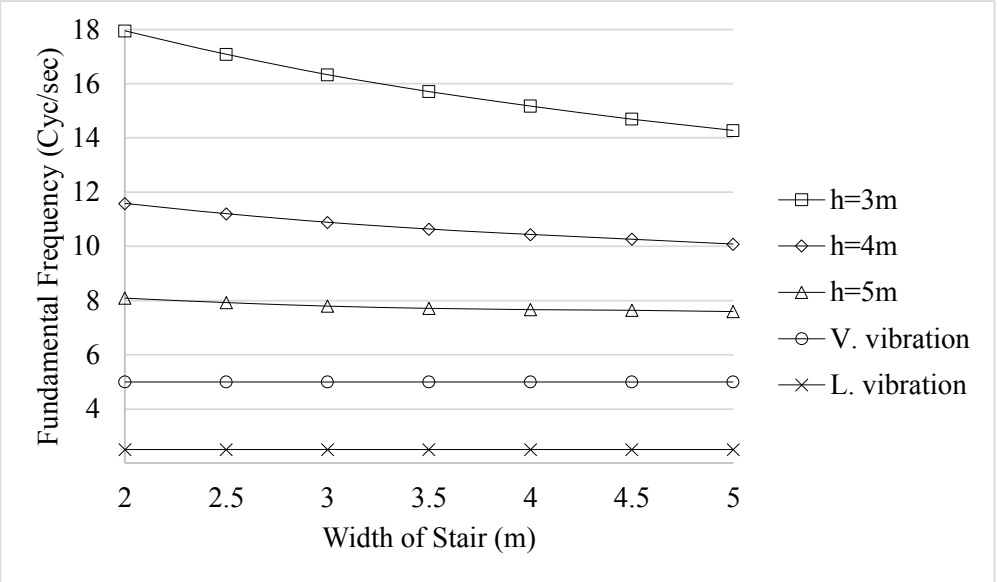

Fig. 6: The Relation Between Fundamental Frequency and Stair Width to Different Stair Height

According to Euro code, a comfort criteria verification is necessary if the fundamental frequency of the deck is below 5Hz for vertical vibrations and 2.5Hz for horizontal and torsional vibrations. The fundamental frequencies of the models are over 5Hz as shown in Fig. 6, so no comfort criteria verification is necessary.

b) The Critical Combination of Torsion Moment

Aside from ignoring the first combination of dead load and live load since the torsion moment equals zero, we also ignored the second combination, as it is very small when compared with the other combinations, the torsion moment ranges between 0.1 and 0.45 t.m.

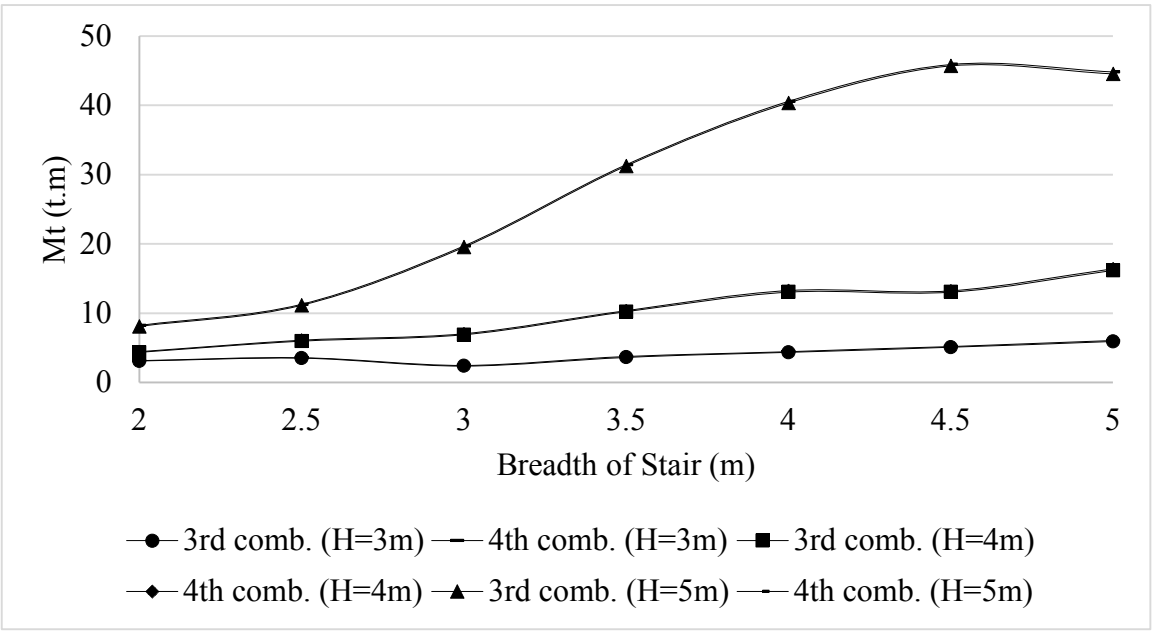

Fig. 7: The Relation Between Torsion Moment and Breadth of Stair With Various Height

A relationship between torsion moment and stair breadth is shown in figure 7, where the breadth ranges from (2m - 5m) and the heights range from (3m - 5m). According to the values, the third and fourth combinations are not significantly different, with the fourth combination being 0.54% to 3.66% larger.

The average torsion moment increases by 7.5% with an increase of 25% from the original breadth for H=3, 19.1% for H=4 and 23.2% for H=5m. Additionally, it is increased by 37.28%, 43.63%, 64.63%, 65.5%, 66.86%, 65.96%, 63.29% for b=2, 2.5, 3, 3.5, 4, 4.5 and 5 m. This corresponds to an increase of 33% from the original height.

c) The critical combination of bending moment

We disregarded the first and second combinations due to small values; values range from 1.3 t.m to 5.7 t.m for these combinations.

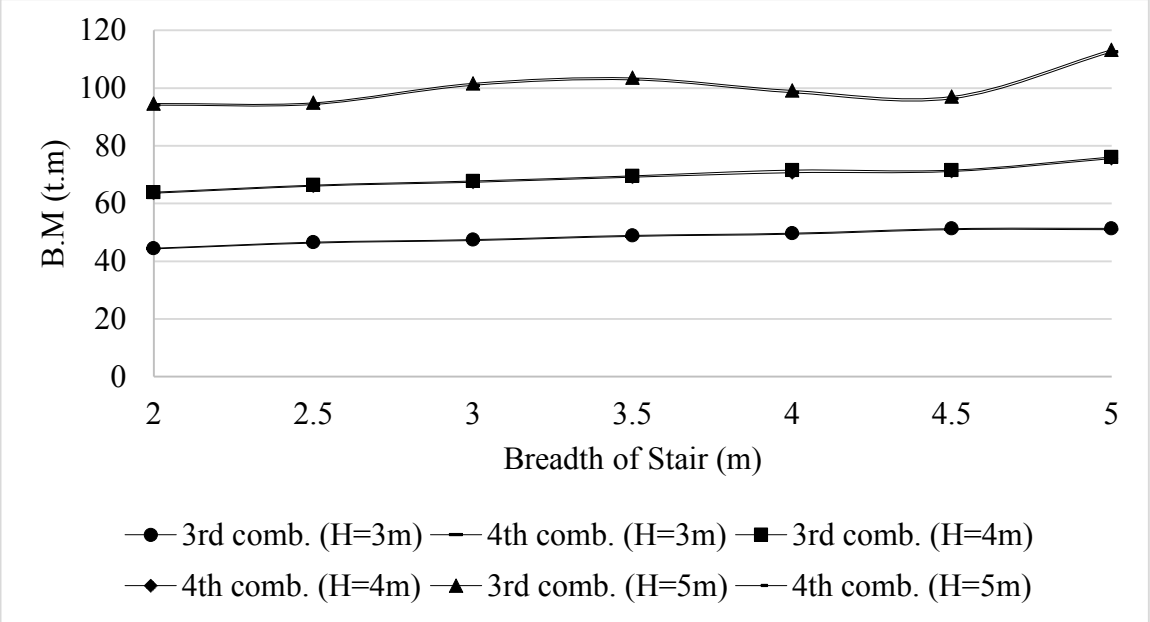

Fig. 8: The Relation Between Bending Moment and Breadth of Stair With Various Height

Fig. 8 shows that there is no difference between the third and the fourth combination, and based on the values, the third combination is bigger than the fourth combination by ranged values from 0.54% to 1.3%. Based on a 25% increase in stair width, the average increase in bending moments is 2.6%. In addition, bending moments increase with stair height; based on a 33% increase in height, the average increase is 30.5%.

d) The critical combination of shear force

As compared to the other values of the third and fourth combinations, the first and second combinations have small values; ranging from 1.1 to 4.4 t.

According to figure 9, the shear force varies with stair width, which ranges between (2-5m) and different stair heights (3-5m). There is no significant difference between the third and fourth combinations, but the third combination ranges from 1% to 1.6% higher than the fourth. In the case of stair heights 3 and 4 m, shear force increases somewhat, but at 5 m, the shear force increases 13.2% based on a 25% increase over the original breadth. Moreover, it increases proportionally with the

height of the stairs, with an average increase of 20.72%, 25.13%, 27.57%, 31.64%, 30%, 33.1% and 36.1%, based on an original height increase of 33%.

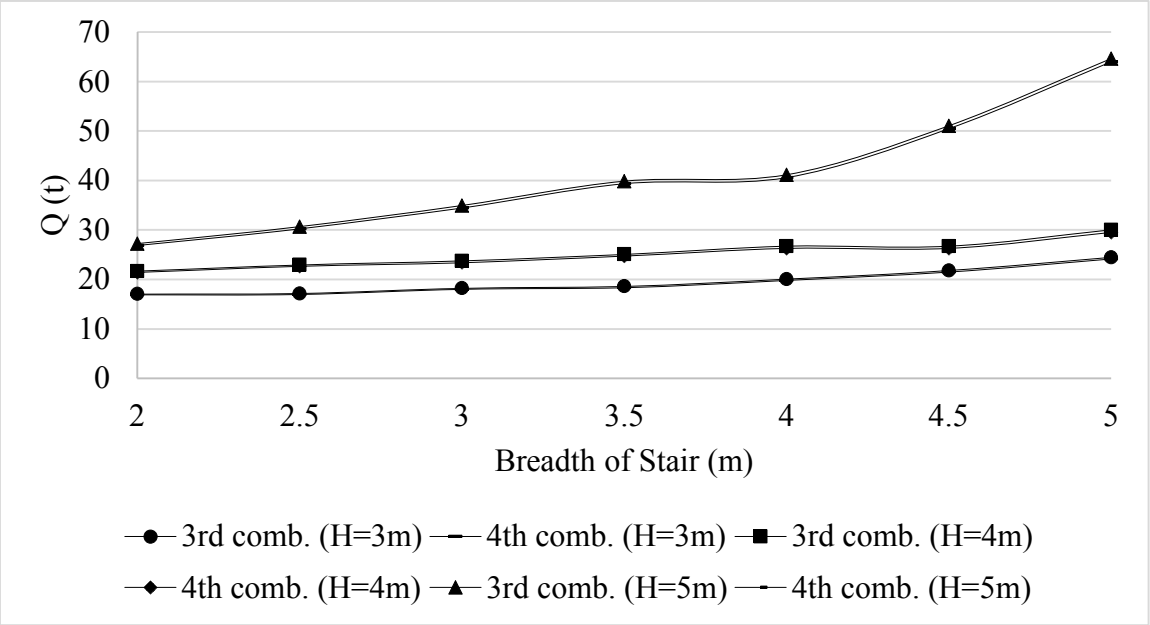

Fig. 9: The Relation Between Shear Force and Breadth of Stair With Various Height

The following equations (Eqs. 3-11) in table (4) show the regression equations for determining the internal forces of beams of varying heights and breadths

Table 4: Regression Equations for Internal Forces of the Beam

H	Internal force	R^2	
3m	$Mt = -1.2716x^6 + 27.549x^5 - 244.54x^4 + 1136.5x^3 - 2911.3x^2 + 3889.6x - 2110.7$	1	*Eq. 3*
	$BM = -1.1277x^6 + 23.548x^5 - 201.58x^4 + 904.86x^3 - 2244.9x^2 + 2919.1x - 1509.1$	1	*Eq. 4*
	$V = 0.8903x^6 - 18.975x^5 + 165.64x^4 - 757.01x^3 + 1908.1x^2 - 2511.1x + 1363$	1	*Eq. 5*
4m	$Mt = 1.9333x^5 - 33.244x^4 + 222.64x^3 - 724.47x^2 + 1147.8x - 704.32$	1	*Eq. 6*
	$BM = 1.0251x^6 - 20.15x^5 + 161.56x^4 - 675.71x^3 + 1553.5x^2 - 1856.6x + 962.86$	1	*Eq. 7*
	$V = 0.8015x^6 - 15.755x^5 + 126.3x^4 - 528.32x^3 + 121.6x^2 - 1458.4x + 732.95$	1	*Eq. 8*
5m	$Mt = -1.3218x^6 + 28.076x^5 - 243.64x^4 + 1100x^3 - 2710.6x^2 + 3456.9x - 1778.5$	1	*Eq. 9*
	$BM = -0.2976x^5 + 11.379x^4 - 117.77x^3 + 514.13x^2 - 1002.8x + 813.34$	1	*Eq. 10*
	$V = -4.8352x^6 + 99.789x^5 - 840.77x^4 + 3700.3x^3 - 8968.5x^2 + 11355x - 5842$	1	*Eq. 11*

x is the breadth of stair

IV. CONCLUSIONS

The stairs are one of our lives' special structures; perhaps because they carry a heavy live load, or made from a variety of materials, or have different shapes inside and outside of the house.

This search focused on a straight stair with a landing that has one beam in the middle. On the beam, five types of loads are applied: a dead load, a live load applied on one side, a live load applied on both sides, a dynamic load applied for three earthquakes, and a pedestrian load. Analyzing the five combinations of loads led to these conclusions:

1- The maximum torsion moment occurs when a dynamic load is combined with a live load on one side. For maximum shear and bending moments, a dynamic load combined with a live load on both sides is critical.
2- The vibration value of a staircase decreases, as it gets taller and wider.
3- Average torsion moments increase 7.5%, 19.1%, and 23.2% for h=3, 4 and 5m, respectively, corresponding to increased breadths of 25%.
4- According to a 33% height increase, the average torsion moment is 37.28%, 43.63%, 64.63%, 65.5%, 66.86%, 65.96% and 63.29% for b=2, 2.5, 3, 3.5, 4, 4.5, 5 m.
5- For a 25% increase in breadth, the average increase in bending moment is 2.6% for all heights, and for a 33% increase in height, the average increase is 30.5% for all breadths.
6- A 25% increase in breadth results in an average increase of 5.5% in shear force for H = 3 m and H = 4 m, and 13.2% for H = 5 m.
7- Based on an increase of 33% from the original height, the average shear force increase for b = 2, 2.5, 3, 3.5, 4, 4.5 and 5 m is 20.72%, 25.13%, 27.57%, 31.64%, 30%, 33.1% and 36.1%.
8- The equations in table (1) enable the designer engineer to calculate the internal forces of the supporting beam.

ACKNOWLEDGEMENTS

I would wish to state my gratitude to ALLAH for giving me the will to accomplish this work. My special thanks and admiration go to Professor Dr Sherif Ahmed Mourad, Professor of Steel Structures and Bridges of the Civil Engineering Department, Faculty of Engineering, Cairo University, Egypt, for his outstanding and sincere assist and valuable advice during the period of this study.

hlmData availability

Some or all data, models, or code that support the findings of this study are available from the corresponding author upon reasonable request.

Declaration of Interest Statement

We have no conflicts of interest to disclose.

Notation

F	The vertical pulsating force.	N
F_o	The reference amplitude of the applied fluctuating force.	N
k (f_v)	A combined factor to deal with (a) the effects of a more realistic pedestrian population, (b) harmonic responses and (c) relative weighting of pedestrian sensitivity to response.	
γ	A reduction factor to allow for the unsynchronized combination of actions in a pedestrian group, a function of damping and effective span.	
N	The number of pedestrians in the group.	
f_v	The natural frequency of the vertical mode under consideration.	Hz
t	Elapsed time.	Sec.
w	Vertical pulsating distributed load	N/m^2
ρ	Crowd density	persons/m^2
S	The span of the bridge	m
b	The width of the bridge subject to pedestrian loading	m
λ	A factor that reduces the effective number of pedestrians when loading from only part of the span contributes to the mode of interest. $\lambda = 0.634(S_{eff}/S)$.	

REFERENCES

1. Abdeldayem Hadhood, Mohammed Gamal Gouda, Mohamed H. Agamy, Hamdy M. Mohamed and Alaa Sherif 2020. Torsion in concrete beams reinforced with GFRP spirals. Engineering Structures, 206, 110174.
2. ACI 2014. Building Code Requirements for Structural Concrete (ACI 318-14). Farmington Hills, MI: American Concrete Institute.
3. Balazs Rigo and Katalin Bagi 2018. Discrete element analysis of stone cantilever stairs. Meccanica 53, 1571–1589.
4. Bellido, C, Quiroz, A, Panizo A and Torero, J L 2009. Performance Assessment of Pressurized.
5. Stairs in High Rise Buildings. *Fire Technology*, 45, 189–200.
6. Brad Davis and Onur Avci 2015. Simplified Vibration Serviceability Evaluation of Slender Monumental Stairs. *J. Struct. Eng.*, 141(11), 04015017.
7. BS EN 1990:2002+A1:2005, Euro code - Basis of structural design.
8. Christopher Higgins 2009. Prefabricated Steel Stair Performance under Combined Seismic and Gravity Loads. J. Struct. Eng., 135(2), 122-129.
9. Faezeh Jafari and Jalal Akbari 2020. Reliability-based design of reinforced concrete beams for simultaneous bending, shear, and torsion loadings. Frattura ed Integrità Strutturale, 51, 136-150
   https://www.britannica.com/technology/staircase-architecture
   http://www.elevestairs.com/stairs-history.php
   https://ngawest2.berkeley.edu/spectras/369214/searches/341874/edit.
10. Jose Santos, Pedro Andrade and Patricia Escorcio. 2019. Pre-design of laterally supported stair steps. Engineering Structures 182, 51-62.
11. Kandekar, S. B. and Talikoti, R. S. 2018. Study of torsional behavior of reinforced concrete beams strengthened with aramid fiber strips. *International Journal of Advanced Structural Engineering* 10, 465–474.
12. Ke Changren, Wang Hanqin. 2020. Study on seismic performance of frame structure with viscous damping staircase. J. Phys.: Conf. Ser. 1676 012069 doi:10.1088/1742-6596/1676/1/012069.
13. Khaldoun N. Rahal 2001. Analysis and design for torsion in reinforced and prestressed concrete beams. *Structural Engineering and Mechanics*, 11(6), 575-590.
14. Lidia Buda 2017. Assessment of stiffness beams subjected to combined shear and torsion designed using STM. *Procedia Engineering*. 193, 152 – 159.
15. Mahsa Beyzaei and Ehsan Seyedi Hosseininia 2019. A Numerical Investigation on the Performance of the Brick Stair Wall as a Supporting Structure by Considering Adjacent Building. *KSCE Journal of Civil Engineering* 23(4), 1513-1521 .
16. Maurizio Angelillo 2015. Static analysis of a Guastavino helical stair as a layered masonry shell Composite *Structures*, 119, 298–304.
17. Michael Kasperski and Benjamin Czwikla 2011. Men-induced loads on stairs. Proceedings of the 8th *International Conference on Structural Dynamics, EURODYN 2011, Leuven, Belgium*, 4-6 July, 949:956.
18. UK National Annex to Euro code 1: Actions on structures – Part 2: Traffic loads on bridges. NA to BS EN 1991-2:2003, © BSI 2008, ISBN 978 0 580 63216 7.
19. Eurocode 1: Actions on structures - Part 2: Traffic loads on bridges, (CEN, 2003)
20. Wang X. and Hutchinson T.C. 2018. Computational assessment of the seismic behavior of steel stairs. *Engineering Structures*. 166, 376–386.
21. Yuxing, Zhao 2016. Earthquake-Resistant Statically Determinate Stairs in Buildings. *Pract. Period. Struct. Des. Constr.*, 21(4), 04016010.

22. Zenonas Turskis and Birutė Juodagalvienė 2016. A Novel Hybrid Multi-Criteria Decision-Making Model to Assess A Stairs Shape for Dwelling Houses. *Journal of Civil Engineering and Management*. 22(8), 1078–1087.
23. Zia Wadud and Sohrabuddin A 2006. Design Charts for Helicoidal Stair Slabs with Landin at Midspan. *Journal of Structural Engineering* © ASCE, 132(2), 312-320.

Scan to know paper details and author's profile

Investigating Machine Learning Models for Effective Dataset Training in Cardiac Arrest Prediction

Innocent Chukwudi Ekuma, Gideon Ihebuzo Ndubuka, Taofik Oladimeji Azeez, Onyebuchi Chikezie Nosiri, Sixtus A. Okafor, Martha C. Ekedigwe, Chidebere A. Otuu & Onwukamuche K. Chikwado

Alex Ekwueme Federal University

ABSTRACT

Inaccuracy of data coupled with invasiveness in diagnosis of cardiac arrest is an issue of concern in clinical setting. In this study, the identification and prediction of cardiac arrest based on existing data was investigated using Machine learning (ML) algorithms. Three classic models of machine learning (Gradient Boost, Random Forest and XGBoost) models were used.

Numerical variables were encoded using Label Encoder function from Scikit learn using the three models to train the data. A panda was used for data loading. After training, Gradient boosting, Random Forest and XGBoost models possess an accuracy of prediction values of 88, 89 and 85% with and an error prediction values of 23, 20 and 27, respectively. Hence fitting Gradient boosting model is the best machine learning model for training data and prediction of cardiac arrest due to its high accuracy and low error value.

Keywords: artificial intelligence; machine learning; dataset; encode, prediction models.

Classification: DDC Code: 006.312 LCC Code: QA76.9.D343

Language: English

Great Britain Journals Press

LJP Copyright ID: 392943
Print ISSN: 2631-8474
Online ISSN: 2631-8482

London Journal of Engineering Research

Volume 23 | Issue 1 | Compilation 1.0

Investigating Machine Learning Models for Effective Dataset Training in Cardiac Arrest Prediction

Innocent Chukwudi Ekuma[α], Gideon Ihebuzo Ndubuka[σ], Taofik Oladimeji Azeez[ρ], Onyebuchi Chikezie Nosiri[Ↄ], Sixtus A. Okafor[¥], Martha C. Ekedigwe[§], Chidebere A. Otuu[χ] & Onwukamuche K. Chikwado[ν]

ABSTRACT

Inaccuracy of data coupled with invasiveness in diagnosis of cardiac arrest is an issue of concern in clinical setting. In this study, the identification and prediction of cardiac arrest based on existing data was investigated using Machine learning (ML) algorithms. Three classic models of machine learning (Gradient Boost, Random Forest and XGBoost) models were used.

Numerical variables were encoded using Label Encoder function from Scikit learn using the three models to train the data. A panda was used for data loading. After training, Gradient boosting, Random Forest and XGBoost models possess an accuracy of prediction values of 88, 89 and 85% with and an error prediction values of 23, 20 and 27, respectively. Hence fitting Gradient boosting model is the best machine learning model for training data and prediction of cardiac arrest due to its high accuracy and low error value.

Keywords: artificial intelligence; machine learning; dataset; encode, prediction models.

Author α §: Department of Biomedical Engineering, Alex Ekwueme Federal University Teaching Hospital Abakaliki, Nigeria.
σ ρ ¥: Department of Biomedical Engineering, Federal University of Technology Owerri, Nigeria.
ρ: ACE-FUELS, FUTO, Nigeria.
α ρ: Department of Biomedical Engineering, David Nweze Umahi Federal University of Health Sciences, Uburu, Ebonyi State, Nigeria.
Ↄ: Department of Electrical Engineering, Federal University of Technology, Owerri, Nigeria.
χ: (Department of Zoology and Environmental Biology, University of Nigeria, Nsukka, Nigeria.)
ν: (Prosthetics and Orthotics Unit, Federal Medical Center, Owerri, Nigeria).
Correspondence Author: Innocent Chukwudi Ekuma; ORCID: 0000-0002-2843-1887.

I. INTRODUCTION

Artificial intelligence (AI) is a simulation of human intelligence in machines programmed to think and mimic human actions (Seetharam, Kagiyama and Sengupta, 2019). It is a computer system that is able to perform tasks that ordinarily require human intelligence such as receiving perceptions from the environment and performing actions. AI uses machine learning algorithms, heuristics, pattern matching, rules, deep learning, cognitive computing and software (Seetharam*et al.*, 2019). It is, specifically, the ability of computer algorithms to approximate based on input data and deep learning (Nadrljanski and Foster 2022). Artificial intelligence has been deployed in healthcare (Mayo 2016), defence, security surveillance (Retson*et al.*, 2019) to mention a few. These algorithms recognize behaviour patterns and create their own logic (Murdoch and Detsky, 2013).

To gain useful insights and predictions, machine learning models are trained using extensive amounts of input data. Retson*et al* (2018) reported that AI algorithms behave differently from humans with a goal for the algorithm to learn exclusively from the input data and understand what it has been programmed to do and some deep learning algorithms to nature as black boxes; hence the algorithms can predict with extreme precision, but offer little to no

comprehensible explanation to the logic behind its decisions aside from the data and type of algorithm used. A neural network also called artificial neural network (ANN) or multi-layer perceptron (MLP) is a supervised machine learning model that has the ability to represent complex nonlinear relationships in the input data.

It was originally developed to model the biological brain, but diverged to be most effectively used for classification and regression tasks (Rumelhart, Hinton and Williams 1986). AI employs artificial neural network (ANN) to simulate the network of neurons that mimic the human brain so for computer to be able to learn things and make decisions in a humanlike manner (Seetharam*et al.*, 2019;Chandran, 2019). ANNs are created by programming of regular interconnected computers to behave like brain cells as shown in Figure 1.

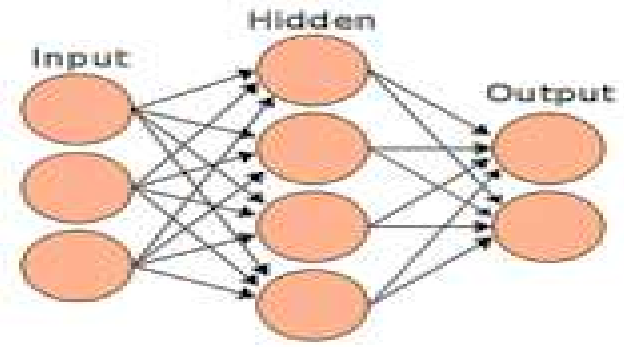

Figure 1: Artificial Neural Network data generated from various interconnected computers (artificial neurons) sent to the (hidden), processed and then displays the information as output (Chandran, 2019)

The development of AI techniques in the sub domains of machine learning and deep learning has attracted the attention of clinicians to create new integrated, reliable and efficient methods for providing quality healthcare delivery (Al-sharqi*et al*, 2018; Chandran, 2019). The techniques have also been deployed in cardiac Computed Tomography for patients with suspected cardiac arrest diseases (CAD). However, machine learning algorithms have shown a potential in clinical practice and training to take non-invasive approaches for detection of functional information beyond atherosclerotic plaque characterization with anomalies (Singh *et al*, 2020). Supervised learning plays an important role not only in the operation of many biological networks but also in operation of artificial neural networks (Seetharam *et al*, 2019).

Moreover, supervised learning has been widely applied to solve many problems. In supervised learning, manually set labels help the machine achieve the desired results. Therefore, supervised learning is applicable to medical diagnosis and treatment, with clinical guiding significance (Narula*et al*, 2016; Nature 2016). Unsupervised learning does not require label of data set, hence the machine must find the label itself.

Furthermore, unsupervised learning algorithms have been successfully implemented in problems such as CVD prediction, diagnosis and treatment, and cardiovascular image analysis (Al-sharqi *et al*, 2018). Reinforcement learning required human to propose a goal and AI to achieve this goal through supervised and unsupervised learning (Li, Hu and Zhang 2017), after which there is a feedback mechanism described as a 'reward' (Seetharam *et al*, 2019).

The aim of reinforcement learning is not to reach the proposed goal, but to maximize the reward for the model during the learning process. This reinforcement learning has been deployed in intensive care units (ICU) to optimize the process by which patients are off mechanical ventilation (Al-sharqi*et al*, 2018; Seetharam *et al*, 2019).

Deep learning (DL) supervised ML technique and characterized by automated algorithms to extract

meaningful patterns from data collections (Krittanawong, Zhang and Wang 2017). It mimics the complexity of a human brain to learn complex hierarchical representations from data that has multiple levels of abstraction (Thomas, Diamond and Vieco, 2018). The programmer enters known data into the machine in a way that allows algorithms to respond correctly even when faced with fully new data.

The neural network learns through experience, reads data, builds hierarchical architectures, and provides advanced input-output levels. It captures complex non-linear relationships between input-output variables. The average error of outcomes and their predictions can be minimized by estimating the weights of input and outcome data (Johnson, Torres and Glicksberg 2018). DL plays a prominent role in Facebook's image recognition program, speech recognition in Apple's Siri and Amazon's Alexa, Google brain and robots to mention a few (Jiang, Jiang and Zhi, 2017). In the medical context, the most widespread deep learning algorithms are convolution neural networks (CNN), recurrent neural networks, deep belief networks, and deep neural networks (Kulkarni and Vijaykumar, 2016). In this work, identifying and predicting cardiac arrest using Machine learning (ML) algorithms was investigated.

II. MATERIALS AND METHODS

2.1 Encoding of Input Variables as Numerical Values

The input data such as age, sex, chest pain type, resting blood pressure, cholesterol level, fasting blood sugar, maximum heart rate, exercise induce angina, oldpeak, slope of the peak ST segment and cardiac arrest datawere trained. The variable were encoded to numerical values using Label Encoder function from Scikit learn which assigned numeric values to each of the variable.

2.2 Dataset Preparation

A Panda was employed to load the dataset and checked for any missing values. If feature is in the right data type as shown in Table 1, the code snippet used to retrieve information from the dataset.

Table 1: Code Snippet Used to Retrieve Dataset Information

```
# check for importantant information
heart.info()
```

```
<class 'pandas.core.frame.DataFrame'>
RangeIndex: 918 entries, 0 to 917
Data columns (total 12 columns):
 #   Column          Non-Null Count  Dtype
---  ------          --------------  -----
 0   Age             918 non-null    int64
 1   Sex             918 non-null    object
 2   ChestPainType   918 non-null    object
 3   RestingBP       918 non-null    int64
 4   Cholesterol     918 non-null    int64
 5   FastingBS       918 non-null    int64
 6   RestingECG      918 non-null    object
 7   MaxHR           918 non-null    int64
 8   ExerciseAngina  918 non-null    object
 9   Oldpeak         918 non-null    float64
 10  ST_Slope        918 non-null    object
 11  CardiacArrest   918 non-null    int64
dtypes: float64(1), int64(6), object(5)
memory usage: 86.2+ KB
```

2.3 Machine Learning Modelling

Trained data was tested by the three tree-based machine learning models (Gradient Boost Model, Random Forest Model and XGBoost Model) using the exact set of data and compared their performances based on their classification report.

III. RESULTS AND DISCUSSION

Fitting gradient boosting model on trained data is presented in Table 1. The classification report of gradient boosting of an accuracy of 88% was obtained. In the gradient boost confusion matrix, the gradient boost model has a true negative and positive values of 69 and 92, whilefalse negative and positive values of 8 and 15, respectively. The summation of true values referto as correct prediction [69+92 = 161] while error prediction value obtained as summation of false values [8 +15 = 23] as presented in Figure 2.

Table 1: Fitting Gradient Boosting on Trained Data

```
# Instantiate the Gradient Boosting model
gradient_boost = GradientBoostingClassifier()

# Fit on the train and test set
gradient_boost.fit(x_train, y_train);
```

```
# Check for performance
performance_check(y_test, x_test, gradient_boost, 'GradientBoost')
```

	precision	recall	f1-score	support
0	0.82	0.90	0.86	77
1	0.92	0.86	0.89	107
accuracy			0.88	184
macro avg	0.87	0.88	0.87	184
weighted avg	0.88	0.88	0.88	184

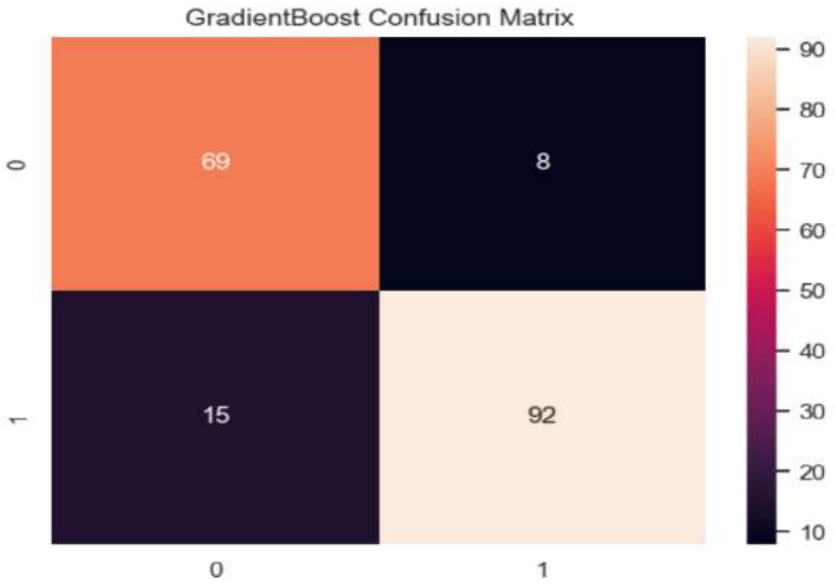

Figure 2: Gradient Boost Confusion Matrix

Table 2 represent fitting random forest model of trained data. Based on the classification reports of trained data, the Random forest gave an accuracy of 89% was obtained. The Gradient boosting for Random forest Confusion matrix as presented in Figure 3 revealed a true negative and positive values of 69 and 95, with false positive and negavive values of 12 and 8, respectively. A coreect prediction value of 164 and an error prediction value of 20 were obtained. Hence, random forest model slightly outperforms the gradient boosting model.

Table 2: Fitting Random Forest on Trained Data

```
RF = RandomForestClassifier()
RF.fit(x_train, y_train);
```

```
# Check for performance
performance_check(y_test, x_test, RF,"RandomForest")
```

```
              precision    recall  f1-score   support

           0       0.85      0.90      0.87        77
           1       0.92      0.89      0.90       107

    accuracy                           0.89       184
   macro avg       0.89      0.89      0.89       184
weighted avg       0.89      0.89      0.89       184

--------------------------------------------------------
```

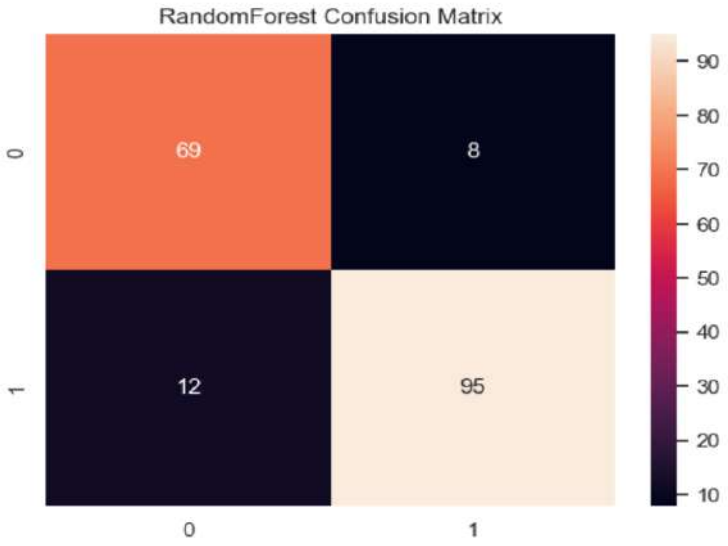

Figure 3: Random Forest Model Confusion Matrix

The XGBoost model classification report shows the accuracy of 85% as shown in Table 3. The accuracy of XGBoost model was found to be less than that of Gradient boost and Random forest models. The XGBoostmodel confusion matrix of trained data revealed a correct prediction of 157 [67+90] with an error prediction value of 27 [10+17] as shown in Figure 4. Thus, Gradient boosting model perform better than XGBoost model in prediction of cardiac arrest.

Table 3: XGBoost Model on Trained Data

```
# Check for performance
performance_check(y_test, x_test, xgb, 'XGBoost')
```

```
              precision    recall  f1-score   support

           0       0.80      0.87      0.83        77
           1       0.90      0.84      0.87       107

    accuracy                           0.85       184
   macro avg       0.85      0.86      0.85       184
weighted avg       0.86      0.85      0.85       184

----------------------------------------------------------
Confusion Matrix
```

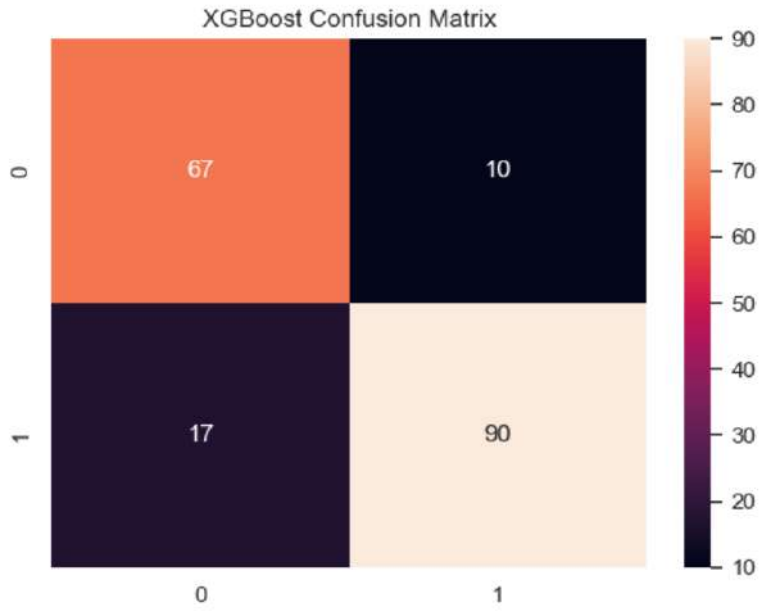

Figure 4: Confusion Matrix of the XGBoost Model

Comparing the three models of machine learning on trained data, Random forest model perform better than Gradient boosting and XGBoost models. This may be attributed to its high accuracy and low error prediction value. It can be deduced during the training period that the machine's output compared to the human provided description of what should be observed.

The three tree-based machine learning models to train data, building on this to analyse data such as age, resting BP, cholesterol, chest pain type, fasting blood sugar, maximum heart rate, exercise induce angina, oldpeak, slope of the peak ST segment to predict the occurrence of cardiac arrest in a given subject. Studies in neuroscience mainly for cardiac arrest correlate human brain to artificial neural network of machine learning models to mimic the brain based on tremendous amount of information for a training set.

IV. CONCLUSION

Based on this study, the following can be drawn:

- Machine learning algorithm can accurately predict cardiac arrest better than other previous techniques.
- While there are various machine learning techniques for different applications, certain model works better in certain environment or situations.

REFERENCE

1. Al-sharqi, M., Woodward, W. J., Mumith, J. A., Markham, D. C., Upton, R., and Leeson, P. (2018). Artificial intelligence and echocardiography. *Echo Research and Practice*, 5, 115 – 125.
2. Chandran, A. (2019). How artificial neural networks work, from the math up. *Berlely* Scientific *Journal*, 6, 123-127.
3. Jiang, F., Jiang, Y. & Zhi, H. (2017). Artificial intelligence in healthcare: past, present and future. *Stroke and Vascular Neurology*, 2 (4), 230–243.
4. Johnson, K.W., Torres, S. J. & Glicksberg, B. S. (2018). Artificial intelligence in cardiology. *Journal of American of College of Cardiology*, 71, 2668–2679.
5. Krittanawong, C., Zhang, H. & Wang, Z. (2017). Artificial intelligence in precision cardiovascular medicine. *Journal of American College Cardiology*, 69, 2657–2664.
6. Kulkarni, A. and Vijay kumar, S. (2016). Application of Internet of Things in artificial heart pacemakers and its impact on security. *International Journal of Current Trends in*

Engineering & Research (IJCTER), 2 (5), 604–610.
7. Li, C., Hu, X. & Zhang, L. (2017). The IoT-based heart disease monitoring system for pervasive healthcare service. *Procedia Computer Science*, 112, 2328–2334.
8. Mayo Clinic, (2016). Heart disease - tests and diagnosis Retrieved from: http://www.mayoclinic.org/diseases-conditions/heart-disease/basics/tests-diagnosis/con-20034056.Accessed on November, 2022.
9. Murdoch, T. B. & Detsky, A. S. (2013). The inevitable application of big data to health care. *Journal of the American Medical Association*, 309 (13), 1351-1352.
10. Nadrljanski, M. & Foster, T. (2022). Computed tomography. Radiopaedia. org. (accessed on 10 Nov 2022) https://doi.org/10.53347/rID-90 27.
11. Narula, S., Shameer, K., Omar, A. M. S., Dudley, J. T. & Sengupta, P. P. (2016). Machine-learning algorithms to automate morphological and functional assessments in 2D echocardiography. *Journal of the American College of Cardiology*, 68 (21), 2287–2295.
12. Nature (2016). Anticipating artificial intelligence. *Nature*, 532, 413.
13. Retson, T. A., Besser, A. H., Sall, S., Golden, D. & Hsiao, A. (2019). Machine learning and deep neural networks in thoracic and cardiovascular imaging. *Journal of Thoracic Imaging*, 34 (3), 192–201.
14. Rumelhart, D. E., Hinton, G. E. & Williams, R. J. (1986). Learning representations by back-propagating errors. *Nature*, 323 (6088), 533–536.
15. Seetharam, K., Kagiyama, N. & Sengupta, P. P. (2019). Application of mobile health, telemedicine and artificial intelligence to echocardiography. *Echo Research and Practice*, 6 (2), 41–52.
16. Singh, D. (2020). Holter monitoring.Cadence Heart Centre. Retrieved from https://cadenceheart.sg/service/holter-monitoring/Accessed November, 2022.
17. Thomas, H., Diamond, J. & Vieco, A. (2018). Global atlas of cardiovascular disease 2000-2016: the path to prevention and control. *Global Heart*, 13, 143–163.

Identification of Mechanical Peroperties of Composite Plates using a Non-Destructive Fast Convergence Method

M. M. Navardi

University of Technology

ABSTRACT

The main purpose of this study is to extract the material properties of a composite plate. Hence, a non-destructive fast convergence method has been proposed to achieve this aim. In this regard, the free vibration test data is first measured using modal analysis. Using the differential quadrature method (DQM) based on first-order deformation theory (FSDT), a standard eigenvalue problem is then provided to calculate natural frequencies. The genetic algorithm is then coupled with the differential quadrature method to find the material properties of a composite plate. Finally, the obtained results are compared and validated with available results in the literature, which show high accuracy and a fast convergence rate.

Keywords: composite plate; differential quadrature method; genetic algorithm; non-destructive method; modal analysis.

Classification: DDC Code: 530.41 LCC Code: QC176

Language: English

Great Britain Journals Press

LJP Copyright ID: 392944
Print ISSN: 2631-8474
Online ISSN: 2631-8482

London Journal of Engineering Research

Volume 23 | Issue 1 | Compilation 1.0

Identification of Mechanical Peroperties of Composite Plates using a Non-Destructive Fast Convergence Method

M. M. Navardi

ABSTRACT

The main purpose of this study is to extract the material properties of a composite plate. Hence, a non-destructive fast convergence method has been proposed to achieve this aim. In this regard, the free vibration test data is first measured using modal analysis. Using the differential quadrature method (DQM) based on first-order deformation theory (FSDT), a standard eigenvalue problem is then provided to calculate natural frequencies. The genetic algorithm is then coupled with the differential quadrature method to find the material properties of a composite plate. Finally, the obtained results are compared and validated with available results in the literature, which show high accuracy and a fast convergence rate.

Keywords: composite plate; differential quadrature method; genetic algorithm; non-destructive method; modal analysis.

Author: Department of Aerospace Engineering and Center of Excellence in Computational Aerospace, Amirkabir University of Technology, 424 Hafez Avenue, Tehran 15875-4413, Iran. email:navardimahdi@aut.ac.ir.

I. INTRODUCTION

Many mechanical structures are composed of composite materials in different mechanical, aerospace, and marine industries. Hence, the exact identification of material properties of the composite structure is vital to achieving a safe design because the manufacturing process is effective on final product specifications. There are some destructive methods to obtain material properties of composite structures. The main idea of such methods is based on failure, which these methods are not proper for sensitive industries. Regarding this issue, a non-destructive method was introduced based on modal test data [1-5].

They indicated that such a method is exact and suitable for calculating the material properties of composite plates. High computational cost is the main drawback of this method. Therefore, many researchers have suggested methods to overcome this problem, such as the genetic algorithm, colony algorithm, and PSO algorithm.

The optimization of the fundamental natural frequency was presented by Narita [6] for composite plates. He used the Ritz method for solving governing equations derived from the Kirchhoff–Love theory of plates. The presented results showed high accuracy in reducing the search time and computational cost [6]. Apalak et al. [7-8] optimized the maximum fundamental frequency of composite plates. They derived the governing equation based on classical theory. The optimal stacking sequences of thin laminated composite plates were searched utilizing the Genetic Algorithm, which combined with an artificial neural network model based on FEM. However, the mentioned optimization methods are known as powerful tools; a suitable computational method, such as finite element method, differential quadrature method, etc., should be used to the reduction of computational cost because of their positive features, including fast convergence and high accuracy

London Journal of Engineering Research

[9-12]. In this regard, Shahverdi et al. [13] introduced a fast convergence method to calculate layups that led to the maximum fundamental frequency in free vibration analysis. Also, they obtained a layup that led to postponed flutter phenomena. They coupled the differential quadrature method with the genetic algorithm based on the first-order deformation theory to achieve these aims. The obtained results showed that the introduced method is an exactly fast convergence method for solving optimization problems.

In the present study, a coupled genetic algorithm method with the Generalized Differential Quadrature (GDQ) method is implemented to obtain the material properties of a composite plate. For this purpose, the governing equations are extracted based on the first shear deformation theory of plates. Also, the eight natural frequencies are obtained using an analysis modal to define the objective function based on these frequencies. The obtained results are evaluated with the available results in the literature.

II. GOVERNING EQUATIONS

The governing equations for a plate based on the first shear deformation theory of is defined by [13-14]:

$$\begin{aligned}
&\frac{\partial N_{xx}}{\partial x}+\frac{\partial N_{xy}}{\partial x}-I_0\ddot{u}_0-I_1\ddot{\phi}_x=0\\
&\frac{\partial N_{yy}}{\partial y}+\frac{\partial N_{xy}}{\partial y}-I_0\ddot{v}_0-I_1\ddot{\phi}_y=0\\
&\frac{\partial}{\partial x}\left(N_{xx}\frac{\partial w_0}{\partial x}\right)+\frac{\partial}{\partial y}\left(N_{yy}\frac{\partial w_0}{\partial y}\right)+\frac{\partial}{\partial y}\left(N_{xy}\frac{\partial w_0}{\partial x}\right)\\
&+\frac{\partial}{\partial x}\left(N_{xy}\frac{\partial w_0}{\partial y}\right)+\frac{\partial Q_x}{\partial x}+\frac{\partial Q_y}{\partial y}-I_0\ddot{w}_0=0\\
&\frac{\partial M_{xx}}{\partial x}+\frac{\partial M_{xy}}{\partial y}-Q_x-I_2\ddot{\phi}_x-I_1\ddot{u}_0=0\\
&\frac{\partial M_{yy}}{\partial y}+\frac{\partial M_{xy}}{\partial x}-Q_y-I_2\ddot{\phi}_y-I_1\ddot{v}_0=0
\end{aligned} \tag{1}$$

where

$$\begin{Bmatrix} I_0\\ I_1\\ I_2 \end{Bmatrix}=\int_{-\frac{h}{2}}^{\frac{h}{2}}\rho\begin{Bmatrix} 1\\ z\\ z^2 \end{Bmatrix}dz \tag{2}$$

where M_x, M_y and M_{xy} are the components of out-of-plate moment. q and ρ denote the intensity of transverse distributed load and the plate mass density per unit area, respectively. N_x, N_y and N_{xy} dente the component of in-plane forces. Q_x and Q_y are the transverse force resultant. Also, w_0 and (I_0, I_1, I_2) denote the transvers displacement and the plate's mass moment of inertia.
Based on the first shear deformation theory of plates, the displacement field of a plate is defined by [13-14]:

$$\begin{aligned}
u(x,y,z,t)&=u_0(x,y,t)+z\phi_x\\
v(x,y,z,t)&=v_0(x,y,t)+z\phi_y\\
w(x,y,z,t)&=w_0(x,y,t)
\end{aligned} \tag{3}$$

where u, v and w denote the displacement component in the x, y and z directions, respectively. u_o and v_o are the in-plane displacement components, and w_o denote the out-of-plane displacement component of the mid-plane of the plate.

the linear strains are expressed by [13-14]:

$$\{\varepsilon\} = \{\varepsilon^0\} + z\{\varepsilon^{(1)}\} \tag{4}$$

where ε^0 and $\varepsilon^{(1)}$ denote the midplane membrane and bending strain vectors [13-14]:

$$\{\varepsilon\} = \begin{Bmatrix} \frac{\partial u_0}{\partial x} \\ \frac{\partial v_0}{\partial y} \\ \frac{\partial w_0}{\partial y} + \phi_y \\ \frac{\partial w_0}{\partial y} + \phi_x \\ \frac{\partial u_0}{\partial y} + \frac{\partial v_0}{\partial x} \end{Bmatrix} + z \begin{Bmatrix} \left(\frac{\partial \phi_x}{\partial x}\right) \\ \left(\frac{\partial \phi_y}{\partial y}\right) \\ 0 \\ 0 \\ \frac{\partial \phi_x}{\partial y} + \frac{\partial \phi_y}{\partial x} \end{Bmatrix} \tag{5}$$

The out-of-plane moments are related to the curvatures through the following relations [13-14]:

$$\begin{Bmatrix} M_{xx} \\ M_{yy} \\ M_{xy} \end{Bmatrix} = \begin{bmatrix} B_{11} & B_{12} & B_{16} \\ B_{12} & B_{22} & B_{26} \\ B_{16} & B_{26} & B_{66} \end{bmatrix} \begin{Bmatrix} \varepsilon^0_{xx} \\ \varepsilon^0_{yy} \\ \gamma^0_{xy} \end{Bmatrix} + \begin{bmatrix} D_{11} & D_{12} & D_{16} \\ D_{12} & D_{22} & D_{26} \\ D_{16} & D_{26} & D_{66} \end{bmatrix} \begin{Bmatrix} \varepsilon^{(1)}_{xx} \\ \varepsilon^{(1)}_{yy} \\ \gamma^{(1)}_{xy} \end{Bmatrix} \tag{6}$$

The out-of-plane moments are related to the curvatures through the following relations [13-14]:

$$\begin{Bmatrix} N_{xx} \\ N_{yy} \\ N_{xy} \end{Bmatrix} = \begin{bmatrix} A_{11} & A_{12} & A_{16} \\ A_{12} & A_{22} & A_{26} \\ A_{16} & A_{26} & A_{66} \end{bmatrix} \begin{Bmatrix} \varepsilon^0_{xx} \\ \varepsilon^0_{yy} \\ \gamma^0_{xy} \end{Bmatrix} + \begin{bmatrix} B_{11} & B_{12} & B_{16} \\ B_{12} & B_{22} & B_{26} \\ B_{16} & B_{26} & B_{66} \end{bmatrix} \begin{Bmatrix} \varepsilon^{(1)}_{xx} \\ \varepsilon^{(1)}_{yy} \\ \gamma^{(1)}_{xy} \end{Bmatrix} \tag{7}$$

where A_{ij} , B_{ij} and D_{ij} denote the extensional stiffnesses , the bending-extensional coupling stiffnesses and the bending stiffnesses , which are associated with the lamina stiffnesses $\bar{Q}_{ij}$ via [13-14]

$$A_{ij} = \int_{-\frac{h}{2}}^{\frac{h}{2}} \bar{Q}_{ij}\, dz \quad ; B_{ij} = \int_{-\frac{h}{2}}^{\frac{h}{2}} \bar{Q}_{ij}.z\, dz \quad ; D_{ij} = \int_{-\frac{h}{2}}^{\frac{h}{2}} \bar{Q}_{ij}.z\, dz \tag{8}$$

Where

$$
\begin{aligned}
\bar{Q}_{11} &= Q_{11}\cos^4\theta + 2(Q_{12}+2Q_{66})\sin^2\theta\cos^2\theta + Q_{22}\sin^4\theta \\
\bar{Q}_{12} &= (Q_{11}+Q_{22}-4Q_{66})\sin^2\theta\cos^2\theta + Q_{12}(\sin^4\theta+\cos^4\theta) \\
\bar{Q}_{22} &= Q_{11}\sin^4\theta + 2(Q_{12}+2Q_{66})\sin^2\theta\cos^2\theta + Q_{22}\cos^4\theta \\
\bar{Q}_{16} &= (Q_{11}-Q_{12}-2Q_{66})\sin\theta\cos^3\theta + (Q_{12}-Q_{22}+2Q_{66})\sin^3\theta\cos\theta \\
\bar{Q}_{26} &= (Q_{11}-Q_{12}-2Q_{66})\sin^3\theta\cos\theta + (Q_{12}-Q_{22}+2Q_{66})\sin\theta\cos^3\theta \\
\bar{Q}_{66} &= (Q_{11}+Q_{22}-2Q_{12}-2Q_{66})\sin^2\theta\cos^2\theta + Q_{66}(\sin^4\theta+\cos^4\theta) \\
\bar{Q}_{44} &= Q_{44}\cos^2\theta + Q_{55}\sin^2\theta \\
\bar{Q}_{45} &= (Q_{55}-\mathrm{Q}_{44})\sin^2\theta\cos^2\theta \\
\bar{Q}_{55} &= Q_{44}\sin^2\theta + Q_{55}\cos^2\theta
\end{aligned}
\tag{9}
$$

where Q_{ij} are the plane stress-reduced stiffnesses, which are defined with young modulus and poison ratio via

$$
\begin{aligned}
Q_{11}^{(k)} &= \frac{E_1^{(k)}}{1-\upsilon_{12}^{(k)}\upsilon_{21}^{(k)}} \quad , Q_{12}^{(k)} = \frac{\upsilon_{12}^{(k)}E_2^{(k)}}{1-\upsilon_{12}^{(k)}\upsilon_{21}^{(k)}} \quad , Q_{22}^{(k)} = \frac{E_2^{(k)}}{1-\upsilon_{12}^{(k)}\upsilon_{21}^{(k)}} \\
Q_{66}^{(k)} &= G_{12}^{(k)} \quad , Q_{44}^{(k)} = G_{23}^{(k)} \quad , Q_{55}^{(k)} = G_{13}^{(k)}
\end{aligned}
\tag{10}
$$

The shear force and the total transverse force components are expressed by [13-14]:

$$
\begin{Bmatrix} Q_y \\ Q_x \end{Bmatrix} = K_s \begin{bmatrix} A_{44} & A_{45} \\ A_{45} & A_{55} \end{bmatrix} \begin{Bmatrix} \gamma_{yz}^0 \\ \gamma_{xz}^0 \end{Bmatrix}
$$

$$
where: \tag{11}
$$

$$
(A_{44},\ A_{45},\ A_{55}) = \int_{-\frac{h}{2}}^{\frac{h}{2}} (\bar{Q}_{44},\ \bar{Q}_{45},\ \bar{Q}_{55})dz
$$

Substituting Eq. (6), Eq. (7) and Eq. (11) into Eq. (1) and neglecting in-plane load, $N(w_0)$, yields [13-14]:

$$A_{11}\left(\frac{\partial^2 u_0}{\partial x^2}\right)+A_{12}\left(\frac{\partial^2 v_0}{\partial y\partial x}\right)+A_{66}\left(\frac{\partial^2 u_0}{\partial y^2}+\frac{\partial^2 v_0}{\partial x\partial y}\right)+B_{11}\left(\frac{\partial^2 \phi_x}{\partial x^2}\right)+B_{12}\left(\frac{\partial^2 \phi_y}{\partial y\partial x}\right)+B_{16}\left(\frac{\partial^2 \phi_x}{\partial x\partial y}+\frac{\partial^2 \phi_y}{\partial x^2}\right)+A_{16}\left(\frac{\partial^2 u_0}{\partial x\partial y}\right)$$
$$+A_{26}\left(\frac{\partial^2 v_0}{\partial y^2}\right)+A_{66}\left(\frac{\partial^2 u_0}{\partial y^2}+\frac{\partial^2 v_0}{\partial x\partial y}\right)+B_{16}\left(\frac{\partial^2 \phi_x}{\partial x\partial y}\right)+B_{26}\left(\frac{\partial^2 \phi_y}{\partial y^2}\right)+B_{66}\left(\frac{\partial^2 \phi_x}{\partial y^2}+\frac{\partial^2 \phi_y}{\partial y\partial x}\right)=I_0\frac{\partial^2 u_0}{\partial t^2}+I_1\frac{\partial^2 \phi_x}{\partial t^2}$$
$$A_{16}\left(\frac{\partial^2 u_0}{\partial x^2}\right)+A_{26}\left(\frac{\partial^2 v_0}{\partial y\partial x}\right)+A_{66}\left(\frac{\partial^2 u_0}{\partial y^2}+\frac{\partial^2 v_0}{\partial x\partial y}\right)+B_{16}\left(\frac{\partial^2 \phi_x}{\partial x^2}\right)+B_{26}\left(\frac{\partial^2 \phi_y}{\partial y\partial x}\right)+B_{66}\left(\frac{\partial^2 \phi_x}{\partial x\partial y}+\frac{\partial^2 \phi_y}{\partial x^2}\right)+A_{12}\left(\frac{\partial^2 u_0}{\partial x\partial y}\right)$$
$$+A_{22}\left(\frac{\partial^2 v_0}{\partial y^2}\right)+A_{26}\left(\frac{\partial^2 u_0}{\partial y^2}+\frac{\partial^2 v_0}{\partial x\partial y}\right)+B_{12}\left(\frac{\partial^2 \phi_x}{\partial x\partial y}\right)+B_{22}\left(\frac{\partial^2 \phi_y}{\partial y^2}\right)+B_{26}\left(\frac{\partial^2 \phi_x}{\partial y^2}+\frac{\partial^2 \phi_y}{\partial x\partial y}\right)=I_0\frac{\partial^2 v_0}{\partial t^2}+I_1\frac{\partial^2 \phi_y}{\partial t^2}$$
$$K_sA_{55}\left(\frac{\partial^2 w_0}{\partial x^2}+\frac{\partial \phi_x}{\partial x}\right)+K_sA_{45}\left(\frac{\partial^2 w_0}{\partial y\partial x}+\frac{\partial \phi_y}{\partial x}\right)+K_sA_{45}\left(\frac{\partial^2 w_0}{\partial x\partial y}+\frac{\partial \phi_x}{\partial y}\right)+K_sA_{44}\left(\frac{\partial^2 w_0}{\partial y^2}+\frac{\partial \phi_y}{\partial y}\right)=I_0\frac{\partial^2 w_0}{\partial t^2}$$
$$B_{11}\left(\frac{\partial^2 u_0}{\partial x^2}\right)+B_{12}\left(\frac{\partial^2 v_0}{\partial y\partial x}\right)+B_{16}\left(\frac{\partial^2 u_0}{\partial y^2}+\frac{\partial^2 v_0}{\partial x\partial y}\right)+D_{11}\left(\frac{\partial^2 \phi_x}{\partial x^2}\right)+D_{12}\left(\frac{\partial^2 \phi_y}{\partial y\partial x}\right)+D_{16}\left(\frac{\partial^2 \phi_x}{\partial x\partial y}+\frac{\partial^2 \phi_y}{\partial x^2}\right)+B_{16}\left(\frac{\partial^2 u_0}{\partial x\partial y}\right) \quad (12)$$
$$+B_{26}\left(\frac{\partial^2 v_0}{\partial y^2}\right)+B_{66}\left(\frac{\partial^2 u_0}{\partial y^2}+\frac{\partial^2 v_0}{\partial x\partial y}\right)+D_{16}\left(\frac{\partial^2 \phi_x}{\partial x\partial y}\right)+D_{26}\left(\frac{\partial^2 \phi_y}{\partial y^2}\right)+D_{66}\left(\frac{\partial^2 \phi_x}{\partial y^2}+\frac{\partial^2 \phi_y}{\partial y\partial x}\right)+K_sA_{55}\left(\frac{\partial w_0}{\partial x}+\phi_x\right)$$
$$-K_sA_{45}\left(\frac{\partial w_0}{\partial y}+\phi_y\right)=I_2\frac{\partial^2 \phi_x}{\partial t^2}+I_1\frac{\partial u_0}{\partial t^2}$$
$$B_{16}\left(\frac{\partial^2 u_0}{\partial x^2}\right)+B_{26}\left(\frac{\partial^2 v_0}{\partial y\partial x}\right)+B_{66}\left(\frac{\partial^2 u_0}{\partial y^2}+\frac{\partial^2 v_0}{\partial x\partial y}\right)+D_{16}\left(\frac{\partial^2 \phi_x}{\partial x^2}\right)+D_{26}\left(\frac{\partial^2 \phi_y}{\partial y\partial x}\right)+D_{66}\left(\frac{\partial^2 \phi_x}{\partial x\partial y}+\frac{\partial^2 \phi_y}{\partial x^2}\right)+B_{12}\left(\frac{\partial^2 u_0}{\partial x\partial y}\right)$$
$$+B_{22}\left(\frac{\partial^2 v_0}{\partial y^2}\right)+B_{26}\left(\frac{\partial^2 u_0}{\partial y^2}+\frac{\partial^2 v_0}{\partial x\partial y}\right)+D_{12}\left(\frac{\partial^2 \phi_x}{\partial x\partial y}\right)+D_{22}\left(\frac{\partial^2 \phi_y}{\partial y^2}\right)+D_{26}\left(\frac{\partial^2 \phi_x}{\partial y^2}+\frac{\partial^2 \phi_y}{\partial y\partial x}\right)+K_sA_{45}\left(\frac{\partial w_0}{\partial x}+\phi_x\right)$$
$$-K_sA_{44}\left(\frac{\partial w_0}{\partial y}+\phi_y\right)=I_2\frac{\partial^2 \phi_y}{\partial t^2}+I_1\frac{\partial u_x}{\partial t^2}$$

III. GENERALIZED DIFFERENTIAL QUADRATURE METHOD

In this section, the formulation of the GDQM is presented. For this aim, the governing equations of a plate in the form of Eq. (12) is initially discretized by using the GDQ method. The key of this method is to determine the derivative of a function with respect to a space variable at a specific point as a weighted linear summation of all the functional values at all other sampling points along the domain [13]. Therefore, the *first* order partial derivative of a function f(x) with respect to the space variable x for the regular domain may be written as:

$$\frac{\partial f(x)}{\partial x}\Big|_{x=x_i}=\sum_{k=1}^{N}A_{ik}^{x}f_{kj} \quad (13)$$

where N is the number of sampling points in the domain and $A_{ik}^{(x)}$ is the first-order weighting coefficients to be defined as follows (16):

$$A_{ik}^{x}=\begin{cases}\dfrac{\prod(x_i)}{(x_i-x_k)\prod(x_k)} & i\neq j\\ -\sum_{v=1,v\neq i}^{M}A_{iv}^{(1)} & i=j\end{cases} \quad (14)$$

where

$$\Pi(\xi_i)=\prod_{v=1,v\neq i}^{N}(x_i-x_v)\quad,\quad \Pi(x_i)=\prod_{v=1,v\neq k}^{N}(x_k-x_v) \tag{15}$$

Also, the higher-order weighting coefficients are defined as follows:

$$A_{ik}^{(r)}=\begin{cases} r\left[A_{ii}^{(r-1)}A_{ik}^{(1)}-\dfrac{A_{ik}^{(r-1)}}{x_i-x_k}\right] & i\neq j \\ -\sum_{v=1,v\neq i}^{M}A_{iv}^{(r)} & i=j \end{cases} \tag{16}$$

It should be noted that the weighting coefficients are only dependent on the derivative order and on the number and distribution of sampling points along the domain. A well-known method of defining these points is to use Chebyshev-Gauss-Lobatto point distribution given by [13-14] as:

$$x_i=\frac{1}{2}\left(1-\cos\frac{(i-1)}{(\mathrm{N}-1)}\pi\right),\quad i=1,2,...,N \tag{17}$$

IV. BOUNDARY CONDITIONS

In this section, free boundary condition is presented.

Hence, at edges $x=0$ or $x=a$: $Q^{x}=0, N^{xx}=0, N^{xy}=0, \mathrm{M}^{xx}=0$ and $M^{xy}=0$.
These equations can be written in DQ form as [13]

$$\begin{aligned} &Q^{x}{}_{kj}=0\quad,\mathrm{N}_{kj}^{xx}=0\quad,N_{kj}^{xy}=0\qquad M_{kj}^{xx}=0\ ,\ M_{kj}^{xy}=0\\ &if\quad x=0\rightarrow k=1\\ &if\ x=a\rightarrow k=N \end{aligned} \tag{18}$$

At edges $y=0$ or $y=b$: $Q^{y}=0, N^{yy}=0, N^{xy}=0, \mathrm{M}^{yy}=0$ and $M^{xy}=0$.
These equations can be written in DQ form as [13]

$$\begin{aligned} &Q^{y}{}_{ik}=0\quad,\mathrm{N}^{yy}{}_{ik}=0\quad,N^{xy}{}_{ik}=0\qquad M_{ik}^{yy}=0\ ,\ M_{ik}^{xy}=0\\ &if\quad y=0\rightarrow k=1\\ &if\quad y=b\rightarrow k=M \end{aligned} \tag{19}$$

V. SOLUTION METHODOLOGY

To solve the discretized the governing equations of free vibration problem with applying boundary conditions by generalized differential quadrature method, the combination of discretized equations is essential in which these equations have been expressed by a system of linear equations shown in Eq. (20) [13]

$$\begin{bmatrix} K_{BB} & K_{BD} \\ K_{DB} & K_{DD} \end{bmatrix}\begin{bmatrix} \delta_B \\ \delta_D \end{bmatrix}-\Omega^2\begin{bmatrix} 0 \\ \delta_D \end{bmatrix}=\begin{bmatrix} 0 \\ 0 \end{bmatrix} \tag{20}$$

where the subscripts B and D denote the boundary and interior points along the domain, respectively. K_{BB}, K_{BD}, K_{DB} and K_{DD} imply the influence coefficients appeared in the discretized equations. δ_B is the

degree of freedom vector including transverse displacements and slope states which considered on the boundaries of domain and defined by: [13]

$$\delta_B = \begin{pmatrix} \{w\}_B \\ \{\psi^x\}_B \\ \{\psi^y\}_B \end{pmatrix} \tag{21}$$

Also, δ_D is the degree freedom vector including transverse displacement of the interior points along a domain and defined by: [13]

$$\delta_D = \{w\}_D \tag{22}$$

Computing δ_D from the first row of Eq. (39) and substituting it into the second row results in the following relation. [13]

$$K\delta_D = \Omega^2 \delta_D \tag{23}$$

Where

$$\begin{aligned} \delta_B &= -K_{BB}^{-1} K_{BD} \delta_D \\ K &= K_{DD} - K_{DB} K_{BB}^{-1} K_{BD} \end{aligned} \tag{24}$$

The Eigen-frequencies of Eq. (20) can be determined through a standard eigenvalue solver.

VI. OPTIMIZATION PROCEDURE

The optimization problem is based on finding those material properties, which is led to the minimum possible objective function. The fibers material properties are behaved as design variables. The optimization problem and the related constraints are expressed as

$$\begin{aligned} &Find \rightarrow \ E_1, E_2, \upsilon_{12}, G_{12}, G_{13} \\ &Minimize \ Objective \quad function \end{aligned} \tag{25}$$

where the objective function is defined as

$$Objective \quad function = \sum_{i=1}^{8} \left(\frac{f_{i\ DQM} - f_{i\ \exp riment}}{f_{i\ \exp riment}} \right)^2 \tag{26}$$

VII. RESULTS AND DISCUSSION

In this section, material properties of a composite plate are extracted by modal test data using the coupled method of genetic algorithm and GDQ method. To achieve this aim, the influence of increasing computational points on natural frequencies has been studies for a fully clamped isotropic plate. Also, the obtained results are then validated with available results in the literature. Finally, the material properties of a composite plate based on convergence of experiment results and present work is calculated.

London Journal of Engineering Research

In order to evaluate the accuracy and fidelity of the present approach, free vibration analysis of a square plate with three different boundary conditions is carried out. Table 1 shows the first five non-dimensional natural frequency of a clamped plate in comparison with those reported in [15] where used Ritz method to determine the non-dimensional natural frequencies. In order to perform the convergence study of the present method, different number of computational points has been considered. The convergence of the results is achieved in 16×16 the sampling point.

Table 1: Non-Dimensional Natural Frequencies of a Square Plate With Clamped Boundary Conditions

Mode sequence					
Method	1	2	3	4	5
[15]	35.992	73.413	73.413	108.270	131.640
Present (8×8)	35.9601	48.2587	60.7376	60.7376	83.3110
Present (10×10)	35.9835	59.9761	74.0714	74.0714	80.8834
Present (11×11)	35.8948	73.3901	73.3901	91.4196	108.2071
Present (12×12)	35.9850	70.4137	73.3705	73.3705	100.3230
Present (14×14)	35.9852	73.3923	73.3923	80.2989	108.0977
Present (16×16)	35.9852	73.3934	73.3934	89.8957	108.1927
Present (18×18)	35.9852	73.3937	73.3937	99.2756	108.2699

Moreover, the first four shape modes of the plate with simply supported edges have been presented in Fig 1.

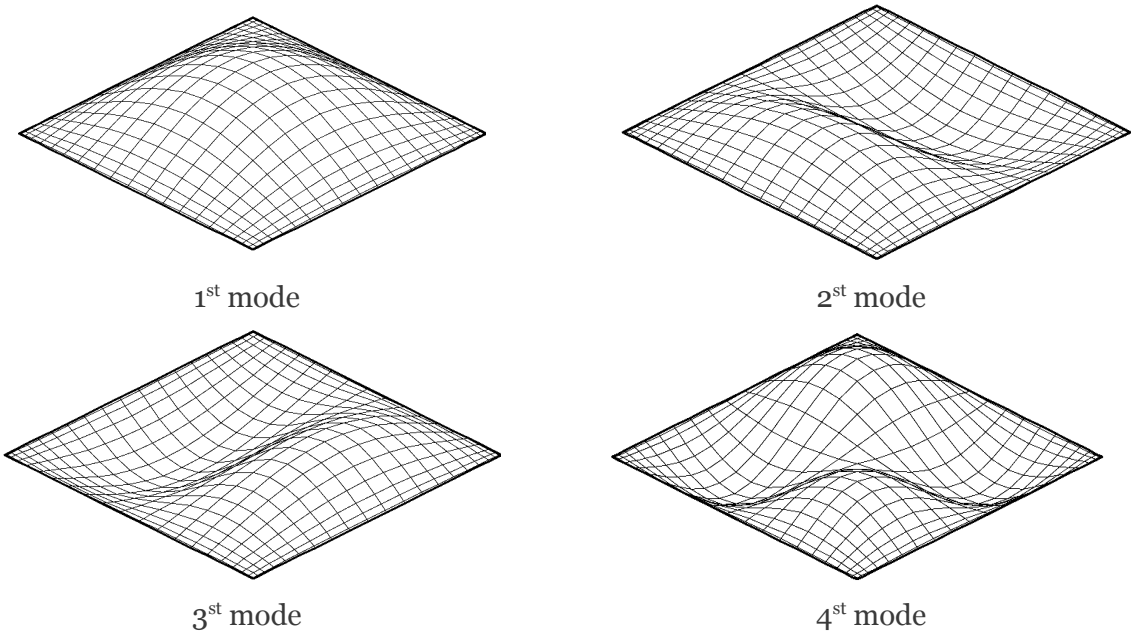

Figure 1: The First Four Mode Shapes of Clamped Square Thin Plate

In the next study, material properties of a composite plate are calculated by using the coupled method of the genetic algorithm with differential quadrature method. In this regard, free vibration data of a composite plate is first done by using modal analysis in which the objective function is calculated based these natural frequencies. The length, width, and thickness of plate is measured 0.25 m, 0.25 m and 0.0028 mm respectively so that the layups orientation of the considered plate is $[0/45]_s$. The lower and upper bound is selected to find material properties of the composite plate according to Eq. (27) .

$$\begin{aligned} 60 \le E_1 \le 150 \\ 1 \le E_2 \le 30 \\ 1 \le G_{12} \le 15 \\ 1 \le G_{13} \le 10 \\ 0.15 \le \upsilon_{12} \le 0.5 \end{aligned} \qquad (27)$$

The material properties of the composite plate are presented by Table 2 that are compared with material peripeties obtained by experimental test.

Table 2: The Physical Parameters of Composite Plate

	$E_{11}(Gpa)$	$E_{22}(Gpa)$	$G_{12}(Gpa)$	$G_{23}(Gpa)$	υ_{12}
present	102.1	8.1	4.2	3.5	0.27
Experimental test	99	7.6	-	-	0.3

The presented results in Table 2 show the accuracy of the present method to calculate material properties of composite plate. The natural frequencies of the composite plate are presented by Table 3 achieved by modal analysis test and the generalized differential quadrature method. The obtained results show good agreement between experimental and numerical methods.

Table 3: Natural Frequencies and Residuals

(Hz)

modes	Experimen	GDQM	Δ %
1	90.2	90.11	0.01
2	131	130.72	0.2
3	223.9	223.42	0.2
4	345	344.73	0.08
5	361	360.99	0.5
6	418	417.92	0.02
7	427.1	426.84	0.06
8	565	563.82	0.7

IIV. CONCLUSIONS

The actual material properties of the composite plate were extracted. The composite plate's governing equations were derived using the first-order deformation theory to achieve this aim. The free vibration of the isotropic plate has been conducted in which the obtained result was compared with available results in the literature to validate the provided discretized equations. The genetic algorithm with the generalized differential quadrature method was coupled to calculate the objective function. Regarding this issue, modal analysis was performed to calculate the objective function based on modal test data. The evaluation of the presented results clarifies the accuracy and convergence of the present method.

REFERENCES

1. Tam, J. H., Ong, Z. C., Ismail, Z., Ang, B. C., & Khoo, S. Y. (2017). Identification of material properties of composite materials using nondestructive vibrational evaluation approaches: A review. *Mechanics of Advanced Materials and Structures*, *24*(12), 971-986.
2. Ragauskas, P., & Belevičius, R. (2009). Identification of material properties of composite materials. *Aviation*, *13*(4), 109-115.
3. Qian, G. L., Hoa, S. V., & Xiao, X. (1997). A vibration method for measuring mechanical properties of composite, theory and experiment. *Composite Structures*, *39*(1-2), 31-38.
4. Mehrez, L., Moens, D., & Vandepitte, D. (2012). Stochastic identification of composite material properties from limited experimental databases, part I: Experimental database construction. *Mechanical Systems and Signal Processing*, *27*, 471-483.
5. Saygili, Y., Genc, G., Sanliturk, K. Y., & Koruk, H. (2022). Investigation of the acoustic and mechanical properties of homogenous and hybrid jute and luffa bio composites. *Journal of Natural Fibers*, *19*(4), 1217-1225.6]] Bellman R, Kashef B. G, Casti, J. Differential quadrature: a technique for the rapid solution of nonlinear partial differential equations. Journal of computational physics 1972; 10.1: 40-52.
6. Narita, Y. (2003) "Layerwise optimization for the maximum fundamental frequency of laminated composite plates", *Journal of Sound and Vibration*, **263**(5), 1005-1016.
7. Apalak, M. K., Yildirim, M., and Ekici, R. (2008), "Layer optimisation for maximum fundamental frequency of laminated composite plates for different edge conditions", *Composites Science and Technology*, **68**(2), 537-550.
8. Apalak, M. K., Karaboga, D., and Akay, B. (2014), "The artificial bee colony algorithm in layer optimization for the maximum fundamental frequency of symmetrical laminated composite plates", *Engineering Optimization*, 46(3), 420-437.
9. Shahverdi, H. and Navardi, M.M. (2017), "Free vibration analysis of cracked thin plates using gene
10. Fantuzzi N. Generalized differential quadrature finite element method applied to advanced structural mechanics. Phd thesis, University of Bologna , Bologna, Italy; 2013.
11. Fantuzzi N, Tornabene F, Viola E. Generalized differential quadrature finite element method for vibration analysis of arbitrarily shaped membranes. International Journal of Mechanical Sciences 2014; 79:216-251.
12. Viola E, Tornabene F, Fantuzzi N. Generalized differential quadrature finite element method for cracked composite structures of arbitrary shape. Composite Structures 2013; 106:815-834.
13. Shahverdi, H., Navardi, M. M., & Khalafi, V. (2021). Optimization of free vibration and flutter analysis of composite plates using a coupled method of genetic algorithm and generalized differential quadrature. *International Journal of Applied Mechanics*, *13*(08), 2150090.
14. Reddy JN. 2004. *Mechanics of laminated composite plates and shells* (CRC press).
15. Leissa AW. 1973. "The free vibration of rectangular plates," *Journal of Sound and vibration* 31,257-293.